nature physics

ARTICLES

PUBLISHED ONLINE: 7 OCTOBER 2012 | DOI: 10.1038/NPHYS2440

Super-elastic collision of large-scale magnetized plasmoids in the heliosphere

Chenglong Shen[1], Yuming Wang[1]*, Shui Wang[1], Ying Liu[2,3], Rui Liu[1], Angelos Vourlidas[4], Bin Miao[1], Pinzhong Ye[1], Jiajia Liu[1] and Zhenjun Zhou[1]

A super-elastic collision is an unusual process in which some mechanism causes the kinetic energy of the system to increase. Most studies have focused on solid-like objects, and have rarely considered gases or liquids, as the collision of these is primarily a mixing process. However, magnetized plasmoids are different from ordinary gases—as cross-field diffusion is effectively prohibited—but it remains unclear how they behave during a collision. Here we present a comprehensive picture of a unique collision between two coronal mass ejections in the heliosphere, which are the largest magnetized plasmoids erupting from the Sun. Our analysis reveals that these two magnetized plasmoids collided as if they were solid-like objects, with a likelihood of 73% that the collision was super-elastic. The total kinetic energy of the plasmoid system increased by about 6.6% through the collision, significantly influencing its dynamics.

Collisional dynamics is essential in determining the global structure and evolution of macro- and micro- objects, such as planet rings[1], granular materials[2] and nanoclusters[3,4]. To classify collisions in terms of energy transfer, Newton defined the coefficient of restitution, e, which is normally between 0 and 1. However, abnormal e values, such as $e > 1$ (refs 2,5–7) or $e < 0$ (refs 4), have been reported. A super-elastic collision is a process through which the linear kinetic energy of the collisional system increases, that is, $|e| > 1$. In the literature, there have been several mechanisms proposed to explain such an abnormal increase in the linear kinetic energy during a collision. In granular physics, for example, the oblique impact collision with local deformation may help transfer rotational kinetic energy into linear kinetic energy[2,4,5] (hereafter kinetic energy refers to linear kinetic energy). Thermal fluctuations are suggested as another possible reason leading to super-elastic collisions of nanoclusters[3].

In the absence of internal magnetic fields, two encountering plasmoids tend to mix together, just like ordinary gases. However, it is unclear what would happen if they carry strong magnetic fields, especially in regards to the nature of the collision and the energy exchange between them. Coronal mass ejections (CMEs) are large-scale[8] magnetized plasmoids, originating from the solar atmosphere and expanding and propagating into the heliosphere. As they are a frequently occurring phenomenon with an occurrence rate of 4–5 CMEs per day during the solar maximum[9], the encounters and interactions between CMEs are unavoidable. Actually, as a consequence of interactions, multiple-interplanetary-CME structures are often observed by *in situ* instruments[10–14]. Thus, the issue of magnetized plasmoid collision may be addressed by investigating observations of CMEs.

However, the CME dynamics in the heliosphere constitute an intricate problem[15–18], especially when the collision/interaction between CMEs is involved[11,19–22]. The dynamics of two successive CMEs of 24–25 January 2007 was discussed in ref. 21, in which four different scenarios were proposed to explain the observations, one of which is a mysterious collision through which the leading CME gained momentum and finally became faster than the overtaking CME. Most recently, a CME–CME interaction event on 1 August 2010 has been intensively studied with a focus on the CME dynamics, CME-driven shock and radio bursts[22–24]. Numerical simulations of the interaction between CMEs have also been carried out by many researchers[25–32], but few discussed the nature of the CME collisions.

During 2–8 November 2008, the Sun Earth Connection Coronal and Heliospheric Investigation (SECCHI) suites[33] onboard the twin Solar Terrestrial Relations Observatories[34] (STEREO) captured the process of the chasing and colliding of two CMEs in the heliosphere with clear imaging observations. Each SECCHI suite carries the cameras COR1, COR2, HI1 and HI2, and can seamlessly track CMEs from the corona to interplanetary space. As the events occurred near the solar minimum, the conditions in the heliosphere were quite simple. The events provide us with a unique opportunity to study the physical details of CME collisions. As will be seen, the collision between the two CMEs is super-elastic in nature, during which their total kinetic energy increased. These results advance our understanding of the behaviour of large-scale magnetized plasmoids.

Imaging of two successive CMEs and their collision

The two CMEs originated from the Sun at about 00:35 UT and 22:35 UT, respectively, on 2 November 2008, when the STEREO-A spacecraft was located at 0.97 AU and 41° to the west of the Sun–Earth line, and STEREO-B was located at 1.07 AU and 40° to the east (Fig. 1a). These events were reported in ref. 35 with a focus on their solar source locations and *in situ* effects at 1 AU. One can refer to that paper or Supplementary Section S2 for the details of the propagation of the two CMEs in the corona. Here we focus on their collision in the heliosphere.

[1]CAS Key Laboratory of Geospace Environment, Department of Geophysics and Planetary Sciences, University of Science and Technology of China, Hefei 230026, China, [2]Space Sciences Laboratory, University of California, Berkeley, California 94720, USA, [3]State Key Laboratory of Space Weather, National Space Science Center, Chinese Academy of Sciences, Beijing 100190, China, [4]Space Science Division, Naval Research Laboratory, Washington DC 20375, USA. *e-mail: ymwang@ustc.edu.cn.

NATURE PHYSICS DOI: 10.1038/NPHYS2440

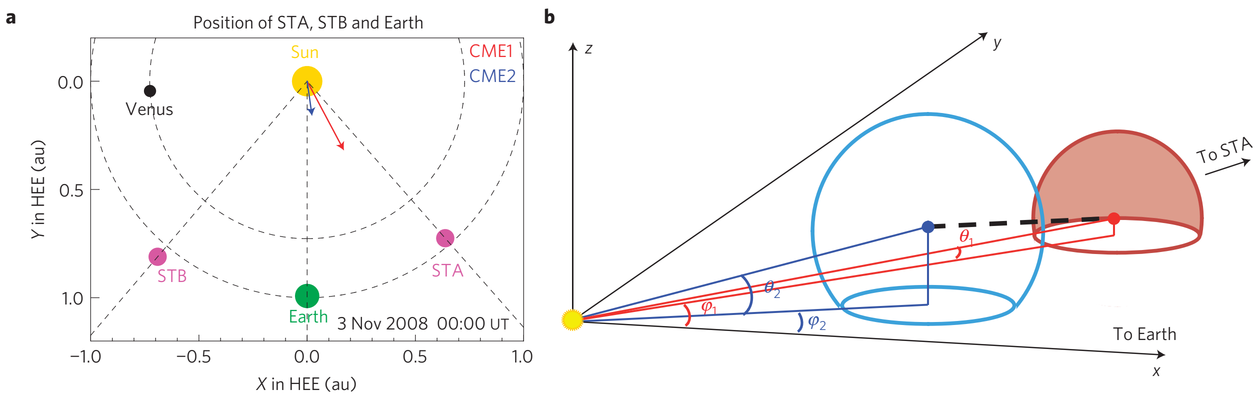

Figure 1 | Configuration of the two CMEs, spacecraft and planets. a,**b**, A sketch map of the positions of the spacecraft (STA, STEREO-A; STB, STEREO-B) in heliocentric Earth ecliptic (HEE) coordinate system (**a**) and the collision of the CMEs (**b**).

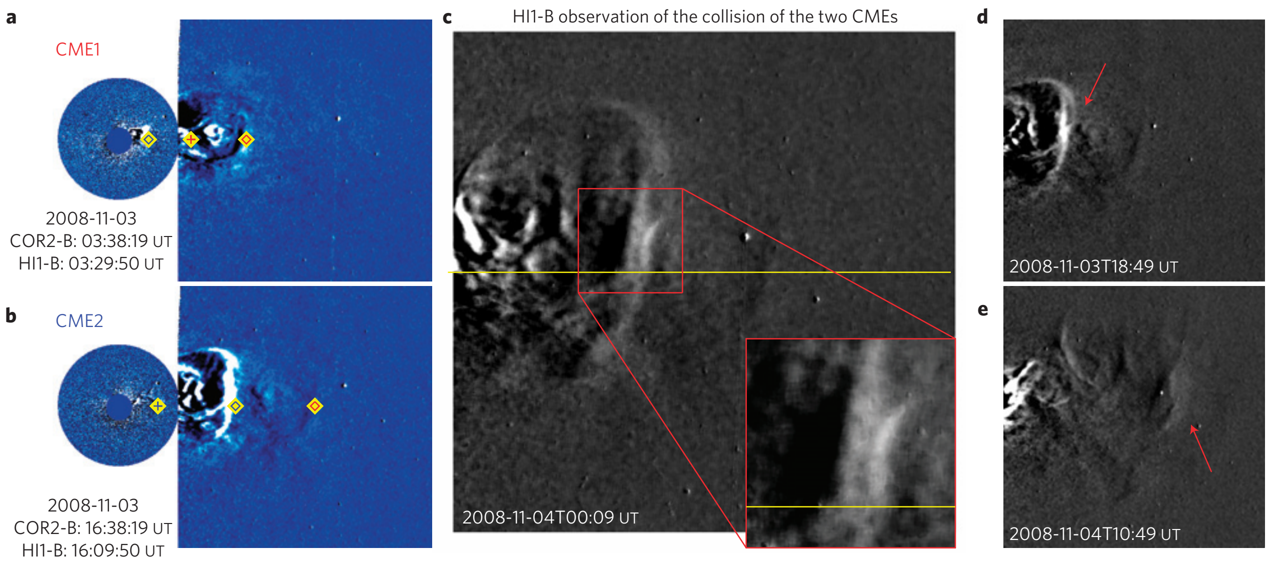

Figure 2 | The STEREO/SECCHI images of the two CMEs and their collision in the heliosphere. a,**b**, Running-difference images showing CME1 and CME2. The red diamond and plus symbols mark the front and rear edges of CME1, respectively, and the blue symbols are for CME2. **c**, The running-difference image of HI1-B showing the collision of the two CMEs. **d**,**e**, The beginning and end of the collision; the red arrows indicate the collision region.

Being faster than CME1, CME2 finally caught up and collided with CME1. This phenomenon was clearly recorded by HI1 onboard STEREO-B, referred to as HI1-B from here. On the basis of the HI1-B images, we can see that the distance between the front edge of CME2 and the rear edge of CME1 became smaller and smaller. The apparent touch of the two CMEs began at approximately 18:49 UT on 3 November 2008, which was registered as a significant enhancement of the brightness around an arc-shaped structure (Fig. 2d). We call the brightness-enhanced region a collision region, and the arc structure is the core of the region. As the arc structure is caving into CME2, the brightness enhancement is not simply due to superposition of the two CMEs, but probably the result of a soft object colliding with a hard object. In fact, if the two CMEs did not collide, the kinetic evolution of CME1 cannot be explained only by solar wind acceleration (see Supplementary Section S11). The brightened arc structure stayed visible for about 7 h with the most clear appearance at around 00:09 UT on 4 November (Fig. 2c). The whole collision region remained brightened much longer until 10:49 UT on 4 November 2008 (Fig. 2e). It seems that the entire collisional process of such large-scale magnetized plasmoids is similar to that of elastic balls, which includes a pre-collision phase, a compression phase, a restitution phase and a post-collision phase. We think that the appearance and disappearance of the visible arc structure define the start and the end of the compression phase, respectively, and the complete disappearance of the brightened region between the two CMEs marks the end of the restitution phase, that is, the end of the collision between them. Movies are available in the Supplementary Information.

Tracking and dynamics of the two CMEs in the heliosphere

To analyse the dynamics of the CMEs and their collision, a time-elongation map, known as a J-map[17,36–38], is constructed. To facilitate the comparison between imaging data and *in situ* data at 1 AU, a 64-pixel-wide slice is placed along the ecliptic plane in the running-difference images from COR2, HI1 and HI2 onboard STEREO-B to produce the J-map (Fig. 3). A bright–dark alternating track from the lower-left to the upper-right usually indicates a bright structure moving away from the Sun. The two vertical dotted green lines mark the start and end times of the collision.

The front edges of CME1 and CME2 are distinct in the J-map as marked by the red and blue diamonds, respectively. They are the same points marked by the red and blue diamond in Fig. 2a,b. The rear edges of the two CMEs are not clear in the J-map. To find out where the tracks of the rear edges of the two CMEs are, we directly identify their rear edges in coronagraph images as done in Fig. 2a,b, and then dot them back to the J-map as shown by the red and blue plus symbols, respectively. Note that the significant track between the red diamond and the plus symbols does not correspond to the CME1's rear edge but to its bright core.

The elongation angle of a given feature in the J-map can be converted to the heliocentric distance under some assumptions[17,38–40]. An often used assumption is to approximate a CME as a sphere[21,32]. By further assuming that the front and rear edges recorded in the J-map are the points of tangency determined by the circular cross-section of the CME in the ecliptic plane and the observer STEREO-B, we get the heliocentric distance of the CME centre, d, its radius, r, and their projected components on the ecliptic plane, d_p and r_p, in terms of the heliocentric distance, l, of STEREO-B, the elongation angles, ε_F and ε_R, of the CME front and rear edges, and the latitude, θ, and longitude, φ, of the CME centre. The detailed derivation can be found in Supplementary Section S4. Owing to the presence of the solar wind stretching effect, a CME might become pancake shaped even if it was initially spherical[41,42]. The HI1 imaging data suggest that the effect is significant for CME2, but not for CME1. Thus, a small correction is made to CME2 to reduce the effect (see Supplementary Section S5).

With the aid of the graduated cylindrical shell model[43,44], the latitude, θ, and longitude, φ, of the two CME centres can be obtained from COR2 images. It is found that both CMEs propagated almost radially with a nearly constant longitude and latitude in the COR2 field of view[35], which are listed in Table 1 (see Supplementary Sections S2 and S3 for details). As the interplanetary magnetic field and solar wind density get weaker and lower, respectively, farther away from the Sun, it is reasonable to assume that they would keep their propagation directions in the HI1 field of view until the collision. The results given by the model suggest that both CMEs propagated between the Sun–Earth line and the Sun–STEREO-A line with CME1 closer to the latter line and CME2 closer to the former, which is in agreement with the previous study[35].

Figure 4 shows d and r as a function of time for both CMEs. As the front and rear edges of the CMEs are more or less diffused, a reasonable error of ±5% in the determination of the elongation angle of the CME front and rear edges is considered. The resultant uncertainties of d and r are indicated by the error bars in Fig. 4. By applying the linear fitting to d and r with these uncertainties taken into account, we get the propagation speed v_c and expansion speed v_e of the two CMEs, as well as their components in the ecliptic plane, v_p and v_{ep}. A 2-σ uncertainty of the speeds derived from the linear fitting is applied in the following analysis. The excellent consistency between the fitting lines and the data points suggests that the two CMEs experienced a nearly constant-speed propagation and expansion in the heliosphere before they met, although a very weak acceleration can be seen for CME1. It should be noted that the uncertainties of CMEs' directions may cause extra uncertainties of CMEs' speeds, and therefore the final values of the uncertainties of CMEs' speeds (see v_c and v_e listed in Table 1) are larger than those given in Fig. 4. Besides, although the front edge of CME2 perhaps travelled faster than the background solar wind, observations suggest that it did not drive an evident shock ahead (see Supplementary Section S12).

Furthermore, in the opposite manner, we derive the elongation angle-time curves from the above results, and plot them on the J-map as white dashed lines in Fig. 3. These white dashed lines are also extrapolated to the post-collision phase. It is found that the fitting lines match the observed tracks very well before the collision, but begin to deviate from the tracks at the beginning of the collision (particularly note the tracks of the two CMEs' front edges). Such deviations mean that the collision between the two CMEs must have significantly changed their propagation directions and/or speeds.

As an attempt, we might as well treat the CMEs approximately as a expanding ball in the collision. The situations of the two CMEs at the time of touching have been sketched in Fig. 1b. It is a collision in three-dimensional space, which should push CME1 closer to the Sun–STEREO-A line in the ecliptic plane and CME2 further away from the ecliptic plane. Thus, it is expected that CME1 would be observed *in situ* by the instruments onboard STEREO-A whereas CME2 would be missed by the *in situ* instruments, which are all located in the ecliptic plane. The *in situ* data at 1 AU do suggest that only CME1 was observed as expected (see Supplementary Section S6 for more details). Its propagation and expansion speeds at 1 AU were about 342 and 30 $km\,s^{-1}$, respectively. The increased propagation speed is consistent with our conjecture that CME1 was accelerated by the collision. The expansion speed is very close to that derived from the J-map. This fact allows us to reasonably assume that the expansion speed was recovered after the collision for both CMEs, although the expansion speed may vary greatly during the collision and CME2 was not locally observed at 1 AU.

Super-elastic collision and the energy exchange

For the case of two expanding elastic balls, not only will their collision result in a momentum exchange in the direction connecting the centroids of the two balls (referred to as the collision direction hereafter), but also their continuous expansion may cause their centroids to separate farther away. We define the approaching speed as the speed of the centroid of one ball relative to the other in the collision direction. Under the assumption that the expansion speeds remained unchanged before and after collision, the collision should be super-elastic if the sum of the expansion speeds of the two balls was larger than the approaching speed before the collision. Here we first show the results for the case of the CMEs' parameters given in Table 1, and then analyse the influence of the uncertainties.

According to the values listed in Table 1, we can derive that the latitude θ_C and longitude φ_C of the collision direction at the beginning of the collision, that is, the elevation angle and azimuthal angle in the heliocentric coordinate system, are about $-10°$ and $57°$, respectively. By resolving the propagation velocity vectors into the components parallel, $v_\parallel$, and perpendicular, $v_\perp$, to the collision direction (see Supplementary Section S7), we find that the values of $v_\parallel$ of the two CMEs were 205 and 237 $km\,s^{-1}$, respectively (listed in Table 1), which give an approaching speed of about 32 $km\,s^{-1}$. The sum of the expansion speeds of the two CMEs was about 117 $km\,s^{-1}$, much larger than the approaching speed. Hence a super-elastic collision is expected.

The conservation of momentum requires $m_1 v_{1\parallel} + m_2 v_{2\parallel} = m_1 v'_{1\parallel} + m_2 v'_{2\parallel}$, where m_1 and m_2 are the mass of CME1 and CME2, respectively, and the prime symbol denotes the parameters after the collision. Here, we approximately treat the collision phase including the compression and restitution phases as a black box, and adopt parameters of the two CMEs before (after) the collision for the first (second) half-period of the collision phase. The influence of this simplification on our final result is not significant (see Supplementary Section S8).

The mass of a CME can be calculated from calibrated coronagraph images[45]. For CME1 and CME2, the derived masses based on COR2-B observations are about 1.8×10^{12} kg and 1.2×10^{12} kg, respectively. The Thomson scattering and projection effects have been corrected[46,47]. The mass ratio of CME1 to CME2 is about 1.5. Hence, for any given coefficient of restitution e, that is, $v'_{2\parallel} - v'_{1\parallel} / v_{1\parallel} - v_{2\parallel}$, the velocities of the two CMEs after the collision can be obtained (see Supplementary Section S7) as well as the expected tracks of the front and rear edges of both the CMEs in the J-map. In fact, our calculation suggests that, no matter which value of the mass ratio we choose, the super-elastic nature of the collision, which will be seen below, does not change (see Supplementary Section S9).

NATURE PHYSICS DOI: 10.1038/NPHYS2440

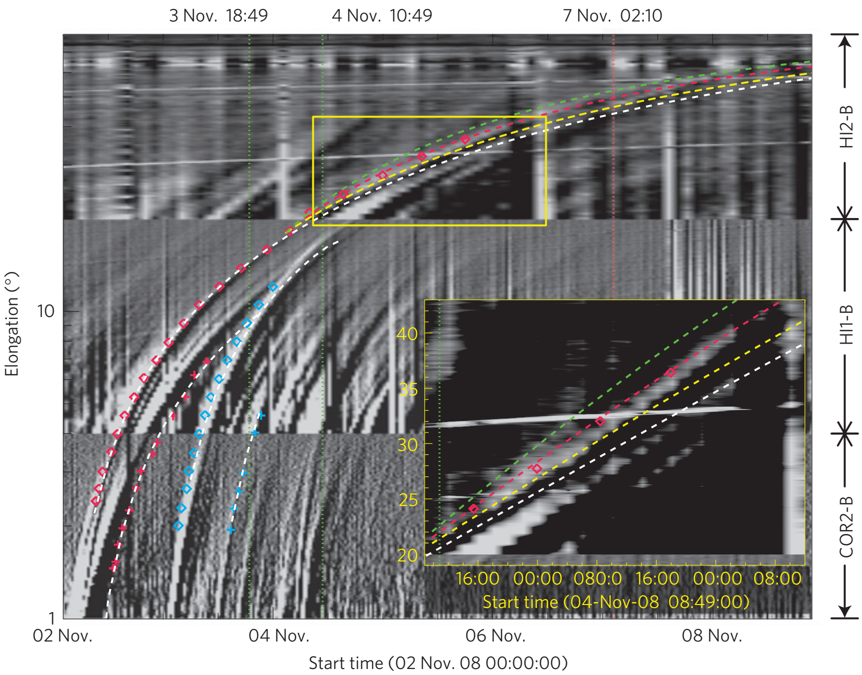

Figure 3 | The time-elongation map from 2 to 9 November 2008 constructed on the basis of the running-difference images from STEREO-B. The diamonds and plus symbols show the front and rear edges of the CMEs, respectively. The two vertical dotted green lines indicate the start and end of the collision. The red vertical line marks the arrival time of CME1 at STEREO-A. The region enclosed by the yellow rectangle is shown at a higher magnification in the lower-right corner. The colour-coded dashed lines are the predicted tracks.

Table 1 | The parameters of the two CMEs before and after the collision.

Parameters derived from observations

	θ	φ	v_c	v_e
CME1	6 ± 2	28 ± 10	243^{+25}_{-16}	43^{+16}_{-15}
CME2	16 ± 2	8 ± 10	407^{+102}_{-74}	74^{+65}_{-51}

Second-level derived parameters

	v_p	v_{ep}	θ_C	φ_C	$v_\perp$	$v_\parallel$	$v'_\parallel$	v'_c	v'_p	v'_{ep}	$\Delta\theta_v$	$\Delta\varphi_v$	$\Delta E/E$	$\Delta E_t/E_t$	e
CME1	241	36			130	205	288	316	316	41	−4	7	68%		
			−10	57										6.6%	5.4
CME2	392	26			332	237	116	351	325	N/A*	6	−16	−25%		

θ and φ are the CME's latitude and longitude. v_c and v_e are the propagation and expansion speed of a CME, derived from the J-map by assuming the CME is a sphere (see Supplementary Sections S4 and S5). v_p and v_{ep} are the average values of the components of v_c and v_e in the ecliptic plane, respectively. θ_C and φ_C are the latitude and longitude of the collision direction (see Supplementary Fig. S7). $v_\perp$ and $v_\parallel$ are the components of the CME velocity perpendicular and parallel to the collision direction, respectively. The superscript prime denotes the parameters after the collision. $\Delta\theta_v$ and $\Delta\varphi_v$ are the change of the CME velocity. $\Delta E/E = (E' - E)/E$ is the percentage of the kinetic energy changed, and E_t is the sum of the kinetic energy of the two CMEs. All of the angles in the table are in units of degrees, and all of the speeds are in units of kilometres per second. Here, only the uncertainties of θ, φ, v_c and v_e are listed, and the uncertainties of speeds have included the uncertainties in the CMEs' directions. The uncertainties of the second-level derived parameters are not listed, but are all taken into account in our analysis. *After the collision, CME2 left the ecliptic plane, and thus there is no available component of expansion speed in the ecliptic plane.

In the J-map, only the track of the front edge of CME1 is still identifiable after the collision. Thus, we repeatedly adjust the value of e to find the best match for the observed track. For the parameters listed in Table 1, the red dashed line starting at the middle of the collision in Fig. 3 shows the best predicted track of the front edge of CME1, which gives $e = 5.4$. As a comparison, the tracks for e equal to 1 and 10 are presented by the yellow and green dashed lines, respectively. A zoomed-in image in the lower-right corner of Fig. 3 presents the details. Obviously, the tracks predicted by both the yellow and green dashed lines get worse. $e = 1$ indicates a perfect elastic collision, but the yellow line is obviously lower than the observed track indicated by the red diamond. The $0 < e < 1$ tracks predicted by our calculation would be located even lower.

As summarized in Table 1, through the collision, CME1 was deflected southwestward and its propagation speed increased from 243 km s^{-1} to about 316 km s^{-1}, whereas CME2 was deflected northeastward and its speed decreased from 407 to 351 km s^{-1}. The *in situ* propagation speed of CME1 was about 40 km s^{-1} larger than the derived post-collision speed of CME1. This is probably due to the continuous acceleration by the solar wind. According to the result, the two CMEs were separating after the collision (see Supplementary Section S10 for a preliminary discussion). It is worth noting that CME2 is completely above the ecliptic plane after the collision. Therefore, it is not surprising that no counterpart of CME2 was detected by *in situ* instruments located in the ecliptic plane. Furthermore, the kinetic energy of CME1 (the contribution from the CME expansion has been taken into account) is found

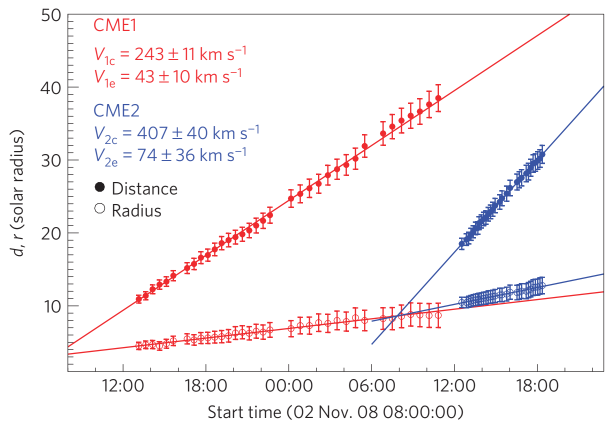

Figure 4 | The heliocentric distance d and the radius r, in units of solar radius, of the two CMEs as functions of time for the case that θ and φ of CME1 are 6° and 28°, respectively, and those of CME2 are 16° and 8°, respectively. The error bars are derived from the 5% uncertainty in the elongation angle. The speeds are obtained by linear fitting with the error bars taken into account, and a 2-σ uncertainty is chosen, which makes the confidence level greater than 95%.

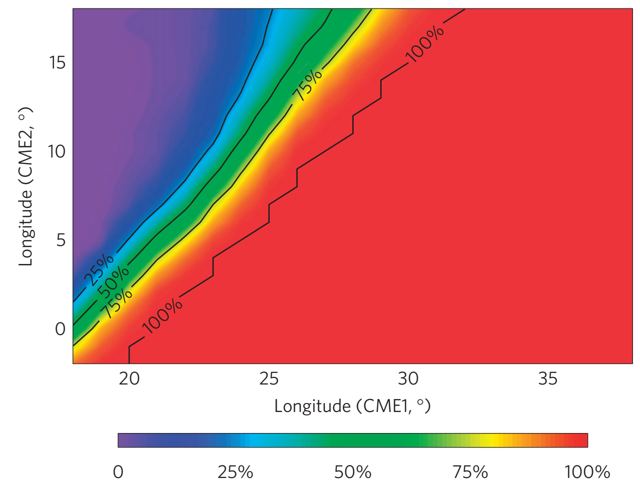

Figure 5 | Likelihood of super-elastic collision calculated by varying the CMEs' longitudes and speeds within their uncertainties. .

to increase by about 68%, whereas that of CME2 decreased by about 25%. As a whole, the system gained about 6.6% kinetic energy during the collision.

The influence of large uncertainties, that is, those in the CMEs' longitudes and velocities as listed in Table 1, is further examined. We sample the longitudes of the two CMEs at 1° within the 10° uncertainty. For each possible pair of longitudes we consider a combination of five propagation speeds, $[v_c \pm \Delta_{vc}, v_c \pm 0.5\Delta_{vc}, v_c]$, for either of both CMEs and five expansion speeds, $[v_e \pm \Delta_{ve}, v_e \pm 0.5\Delta_{ve}, v_e]$, for CME1, which constitute 125 cases. Here, Δ_{vc} and Δ_{ve} are the uncertainties in the CME speeds. For each case we are able to obtain a value of e and the change of the total kinetic energy. The likelihood of super-elastic collision for each longitude pair is therefore calculated. Figure 5 presents the result. Most areas show a strong likelihood of super-elastic collision. Specifically, 72.6% are more than 75% likely, and 63.0% are 100% likely, to experience a super-elastic collision. In contrast, as few as 6.3% combinations are definitely non-super-elastic. Overall, it is 72.8% likely for the collision to be super-elastic.

Source of kinetic energy gain

The source of the net kinetic energy gain and the mechanism of the energy conversion are key issues for super-elastic collisions. The divergent configuration of solar wind implies that the internal pressure of a CME is always stronger than the external pressure when it moves away from the Sun, which is the main cause of the CME expansion. In this process, the magnetic and thermal energies of the CME are continuously dissipated[48,49]. It could be estimated that, for a typical CME at 1 AU with a magnetic field strength of 10 nT, temperature of 10^5 K, density of 5 cm^{-3} and velocity of 500 km s^{-1}, the magnetic and thermal energy density is about 6% of the kinetic energy density. The percentage will be much higher when the CME is closer to the Sun. Thus, the magnetic and thermal energy of CMEs should be sufficient to provide a ∼6.6% increase in the kinetic energy in the super-elastic collision, and the persistent expansion of CMEs may provide the way for the magnetic/thermal energy to convert into kinetic energy.

Besides, the detailed interacting process may also be important in determining the nature of the collision. An anti-correlation between the impact velocity and the coefficient of restitution was reported in collisions among ice particles of Saturn's B ring[1] and granular materials[50]. Experiments and simulations on granular materials and nanoclusters have further shown that the collision between a hard sphere and a soft plate tends to be super-elastic[2,4,5]. These imply that super-elastic collision requires sufficient interaction time and touching area for momentum exchange and energy conversion. In our case, the compression and restitution phases lasted about 16 h, during which a clear arc-shaped structure stayed visible for about 7 h. These phenomena suggest that the two CMEs had sufficient time and a sufficiently large touching area to convert magnetic/thermal energy into kinetic energy. It is worthy of further investigation to examine whether a similar anti-correlation applies to CME collisions, that is, whether a larger coefficient of restitution corresponds to a lower impact velocity.

Although in granular physics, rotational motion and thermal fluctuation have been considered the possible mechanism for the increased kinetic energy[2–5], they are probably not suitable for CME collisions. First, there is no evidence that plasma within a CME undergoes a significant rotation in interplanetary space. Second, CMEs are large-scale structures with huge mass and thus the thermal fluctuation of microscopic particles should not be able to affect the macroscopic behaviour of CMEs.

The good match between the predictions of the simplest collision model and the observations suggests that such large-scale magnetized plasmoids could be simplified as balls instead of using complicated magnetohydrodyanmics or plasma kinetic theories in studying their collision. The collision may be super-elastic, through which the system gains kinetic energy from the magnetic/thermal energy of CMEs. Of course, the process and consequence might be different if significant reconnection occurs in the collision region. This will be another issue.

Received 3 March 2012; accepted 3 September 2012; published online 7 October 2012

References

1. Bridges, F. G., Hatzes, A. & Lin, D. N. C. Structure, stability and evolution of Saturn's rings. *Nature* **309,** 333–335 (1984).
2. Louge, M. Y. & Adams, M. E. Anomalous behavior of normal kinematic restitution in the oblique impacts of a hard sphere on an elastoplastic plate. *Phys. Rev. E* **65,** 021303 (2002).
3. Kuninaka, H. & Hayakawa, H. Simulation of cohesive head-on collisions of thermally activated nanoclusters. *Phys. Rev. E* **79,** 031309 (2009).
4. Saitoh, K., Bodrova, A., Hayakawa, H. & Brilliantov, N. V. Negative normal restitution coefficient found in simulation of nanocluster collisions. *Phys. Rev. Lett.* **105,** 238001 (2010).
5. Kuninaka, H. & Hayakawa, H. Anomalous behavior of the coefficient of normal restitution in oblique impact. *Phys. Rev. Lett.* **93,** 154301 (2004).
6. Smith, C. E. & Liu, P-P. Coefficients of restitution. *J. Appl. Mech.* **59,** 963–969 (1992).

7. Calsamiglia, J., Kennedy, S. W., Chatterjee, A., Ruina, A. & Jenkins, J. T. Anomalous frictional behavior in collisions of thin disks. *J. Appl. Mech.* **66,** 146–152 (1999).
8. Lepping, R. P., Jones, J. A. & Burlaga, L. F. Magnetic field structure of interplanetary magnetic clouds at 1 AU. *J. Geophys. Res.* **95,** 11957–11965 (1990).
9. Yashiro, S. *et al.* A catalog of white light coronal mass ejections observed by the soho spacecraft. *J. Geophys. Res.* **109,** A07105 (2004).
10. Burlaga, L. F., Plunkett, S. P. & St Cyr, O. C. Successive CMEs and complex ejecta. *J. Geophys. Res.* **107,** 1266 (2002).
11. Wang, Y. M., Wang, S. & Ye, P. Z. Multiple magnetic clouds in interplanetary space. *Sol. Phys.* **211,** 333–344 (2002).
12. Wang, Y. M., Ye, P. Z. & Wang, S. Multiple magnetic clouds: Several examples during March–April, 2001. *J. Geophys. Res.* **108,** 1370 (2003).
13. Wang, Y. M., Ye, P. Z., Wang, S. & Xue, X. H. An interplanetary cause of large geomagnetic storms: Fast forward shock overtaking preceding magnetic cloud. *Geophys. Res. Lett.* **30,** 1700 (2003).
14. Farrugia, C. & Berdichevsky, D. Evolutionary signatures in complex ejecta and their driven shocks. *Ann. Geophys.* **22,** 3679–3698 (2004).
15. Wang, Y. *et al.* Impact of the major coronal mass ejections on geo-space during September 7–13, 2005. *Astrophys. J.* **646,** 625–633 (2006).
16. Harrison, R. A. *et al.* Two years of the STEREO heliospheric imagers. Invited review. *Sol. Phys.* **256,** 219–237 (2009).
17. Liu, Y. *et al.* Geometric triangulation of imaging observations to track coronal mass ejections continuously out to 1 AU. *Astrophys. J.* **710,** L82–L87 (2010).
18. Liu, Y., Luhmann, J. G., Bale, S. D. & Lin, R. P. Solar source and heliospheric consequences of the 2010 April 3 coronal mass ejection: A comprehensive view. *Astrophys. J.* **734,** 84 (2011).
19. Gopalswamy, N., Yashiro, S., Kaiser, M. L., Howard, R. A. & Bougeret, J. L. Radio signatures of coronal mass ejection interaction: Coronal mass ejection cannibalism? *Astrophys. J.* **548,** L91–L94 (2001).
20. Shen, C., Wang, Y., Ye, P. & Wang, S. Enhancement of solar energetic particles during a shock-magnetic cloud interacting complex structure. *Sol. Phys.* **252,** 409–418 (2008).
21. Lugaz, N., Vourlidas, A. & Roussev, I. I. Deriving the radial distances of wide coronal mass ejections from elongation measurements in the heliosphere application to CME–CME interaction. *Ann. Geophys.* **27,** 3479–3488 (2009).
22. Liu, Y. D. *et al.* Interactions between coronal mass ejections viewed in coordinated imaging and *in situ* observations. *Astrophys. J.* **746,** L15 (2012).
23. Martínez Oliveros, J. C. *et al.* The 2010 August 01 type II burst: A CME – CME interaction, and its radio and white-light manifestations. *Astrophys. J.* **748,** 66 (2012).
24. Temmer, M. *et al.* Characteristics of kinematics of a coronal mass ejection during the 2010 August 1 CME–CME interaction event. *Astrophys. J.* **749,** 57 (2012).
25. Gonzalez-Esparza, A., Santillán, A. & Ferrer, J. A numerical study of the interaction between two ejecta in the interplanetary medium: one- and two-dimensional hydrodynamic simulations. *Ann. Geophys.* **22,** 3741–3749 (2004).
26. Schmidt, J. & Cargill, P. A numerical study of two interacting coronal mass ejections. *Ann. Geophys.* **22,** 2245–2254 (2004).
27. Wang, Y., Zheng, H., Wang, S. & Ye, P. MHD simulation of the formation and propagation of multiple magnetic clouds in the heliosphere. *Astron. Astrophys.* **434,** 309–316 (2005).
28. Lugaz, N., Manchester, W. B. IV & Gombosi, T. I. Numerical simulation of the interaction of two coronal mass ejections from Sun to Earth. *Astrophys. J.* **634,** 651–662 (2005).
29. Hayashi, K., Zhao, X-P. & Liu, Y. MHD simulation of two successive interplanetary disturbances driven by cone-model parameters in IPS-based solar wind. *Geophys. Res. Lett.* **33,** 20103 (2006).
30. Xiong, M., Zheng, H., Wu, S. T., Wang, Y. & Wang, S. Magnetohydrodynamic simulation of the interaction between two interplanetary magnetic clouds and its consequent geoeffectiveness. *J. Geophys. Res.* **112,** A11103 (2007).
31. Xiong, M., Zheng, H. & Wang, S. Magnetohydrodynamic simulation of the interaction between two interplanetary magnetic clouds and its consequent geoeffectiveness: 2. Oblique collision. *J. Geophys. Res.* **114,** A11101 (2009).
32. Shen, F. *et al.* Three-dimensional MHD simulation of two coronal mass ejections' propagation and interaction using a successive magnetized plasma blobs model. *J. Geophys. Res.* **116,** A09103 (2011).
33. Howard, R. A. *et al.* Sun earth connection coronal and heliospheric investigation (SECCHI). *Space Sci. Rev.* **136,** 67–115 (2008).
34. Kaiser, M. L. *et al.* The stereo mission: An introduction. *Space Sci. Rev.* **136,** 5–16 (2008).
35. Kilpua, E. K. J. *et al.* STEREO observations of interplanetary coronal mass ejections and prominence deflection during solar minimum period. *Ann. Geophys.* **27,** 4491–4503 (2009).
36. Sheeley, N. R. Jr, Walters, J. H., Wang, Y-M. & Howard, R. A. Continuous tracking of coronal outflows: Two kinds of coronal mass ejections. *J. Geophys. Res.* **104,** 24739–24768 (1999).
37. Davies, J. A. *et al.* A synoptic view of solar transient evolution in the inner heliosphere using the heliospheric imagers on STEREO. *Geophys. Res. Lett.* **36,** L02102 (2009).
38. Liu, Y. *et al.* Reconstructing coronal mass ejections with coordinated imaging and *in situ* observations: Global structure, kinematics, and implications for space weather forecasting. *Astrophys. J.* **722,** 1762–1777 (2010).
39. Lugaz, N. Accuracy and limitations of fitting and stereoscopic methods to determine the direction of coronal mass ejections from heliospheric imagers observations. *Sol. Phys.* **267,** 411–429 (2010).
40. Lugaz, N. *et al.* Determining the azimuthal properties of coronal mass ejections from multi-spacecraft remote-sensing observations with STEREO SECCHI. *Astrophys. J.* **715,** 493–499 (2010).
41. Riley, P. & Crooker, N. U. Kinematic treatment of coronal mass ejection evolution in the solar wind. *Astrophys. J.* **600,** 1035–1042 (2004).
42. Liu, Y., Richardson, J. D., Belcher, J. W. & Kasper, J. C. Constraints on the global structure of magnetic clouds: Transverse size and curvature. *J. Geophys. Res.* **111,** A12S03 (2006).
43. Thernisien, A., Howard, R. & Vourlidas, A. Modeling of flux rope coronal mass ejections. *Astrophys. J.* **652,** 763–773 (2006).
44. Thernisien, A. Implementation of the graduated cylindrical shell model for the three-dimensional reconstruction of coronal mass ejections. *Astrophys. J. Suppl. Ser.* **194,** 33 (2011).
45. Vourlidas, A., Subramanian, P., Dere, K. P. & Howard, R. A. Large-angle spectrometric coronagraph measurements of the energetics of coronal mass ejections. *Astrophys. J.* **534,** 456–467 (2000).
46. Hundhausen, A. J. Sizes and locations of coronal mass ejections—SMM observations from 1980 and 1984–1989. *J. Geophys. Res.* **98,** 13177–13200 (1993).
47. Vourlidas, A. & Howard, R. A. The proper treatment of coronal mass ejection brightness: A new methodology and implications for observations. *Astrophys. J.* **642,** 1216–1221 (2006).
48. Kumar, A. & Rust, D. M. Interplanetary magnetic clouds, helicity conservation, and current-core flux-ropes. *J. Geophys. Res.* **101,** 15667–15684 (1996).
49. Wang, Y., Zhang, J. & Shen, C. An analytical model probing the internal state of coronal mass ejections based on observations of their expansions and propagations. *J. Geophys. Res.* **114,** A10104 (2009).
50. Hayakawa, H. & Kuninaka, H. Theory of the inelastic impact of elastic materials. *Phase Transit.* **77,** 889–909 (2004).

Acknowledgements

We acknowledge the use of data from the SECCHI, IMPACT, PLASTIC and WAVES instruments on STEREO, LASCO on SOHO and WAVES on WIND. STEREO is the third mission in NASA's Solar Terrestrial Probes programme, and SOHO is a mission of international cooperation between ESA and NASA. Y.W. also thanks N. Lugaz for some valuable discussion. This work is supported by grants from the 973 key project 2011CB811403, NSFC 41131065, 40904046, 40874075 and 41121003, CAS the Key Research Program KZZD-EW-01, 100-talent program, KZCX2-YW-QN511 and start-up fund, and MOEC 20113402110001 and the fundamental research funds for the central universities.

Author contributions

Y.W. designed the analysis of the collision and performed the theoretical derivations. C.S. found this event and carried out the data processing and calculations. S.W. gave constructive suggestions on the analysis of the collision. Y.L. gave some advice on the construction of the J-map and interpretation of the elongation angle. B.M. carried out the literature investigation and provided valuable additions. A.V. calculated the masses of the CMEs and gave many valuable suggestions. R.L. and P.Y. participated in the discussion and gave many suggestions. J.L. and Z.Z. made a contribution to the data analysis.

Additional information

Supplementary information is available in the online version of the paper. Reprints and permissions information is available online at www.nature.com/reprints. Correspondence and requests for materials should be addressed to Y.W.

Competing financial interests

The authors declare no competing financial interests.

nature physics
SUPPLEMENTARY INFORMATION
DOI: 10.1038/NPHYS2440

Super-elastic collision of large-scale magnetized plasmoids in the heliosphere

Chenglong Shen[1], Yuming Wang[1], Shui Wang[1], Ying Liu[2,4], Rui Liu[1], Angelos Vourlidas[3], Bin Miao[1], Pinzhong Ye[1], Jiajia Liu[1], & Zhenjun Zhou[1]

[1] *CAS Key Laboratory of Geospace Environment, Department of Geophysics and Planetary Sciences, University of Science and Technology of China, Hefei 230026, China*

[2] *Space Sciences Laboratory, University of California, Berkeley, CA 94720, USA*

[3] *Space Science Division, Naval Research Laboratory, Washington, D.C. 20375, USA*

[4] *State Key Laboratory of Space Weather, National Space Science Center, Chinese Academy of Sciences, Beijing, China*

Contents

1 J-map without any legends and decorations **3**

2 Results of GCS Modeling **4**

3 Validating the longitudes of the CMEs **5**

4 Convert elongation angle to heliocentric distance **8**

5 Validity of the assumption of a sphere **9**

6 In situ observations of CME1 at 1 AU **12**

7 Resolution of velocity vectors for the analysis of collision **12**

8 The direction change of the CMEs during the collision **15**

9 Influence of mass ratio on the result **18**

10 Discussion about post-collision phase **18**

11 Momentum coupling with the solar wind **20**

12 Absence of shock ahead of CME2 **22**

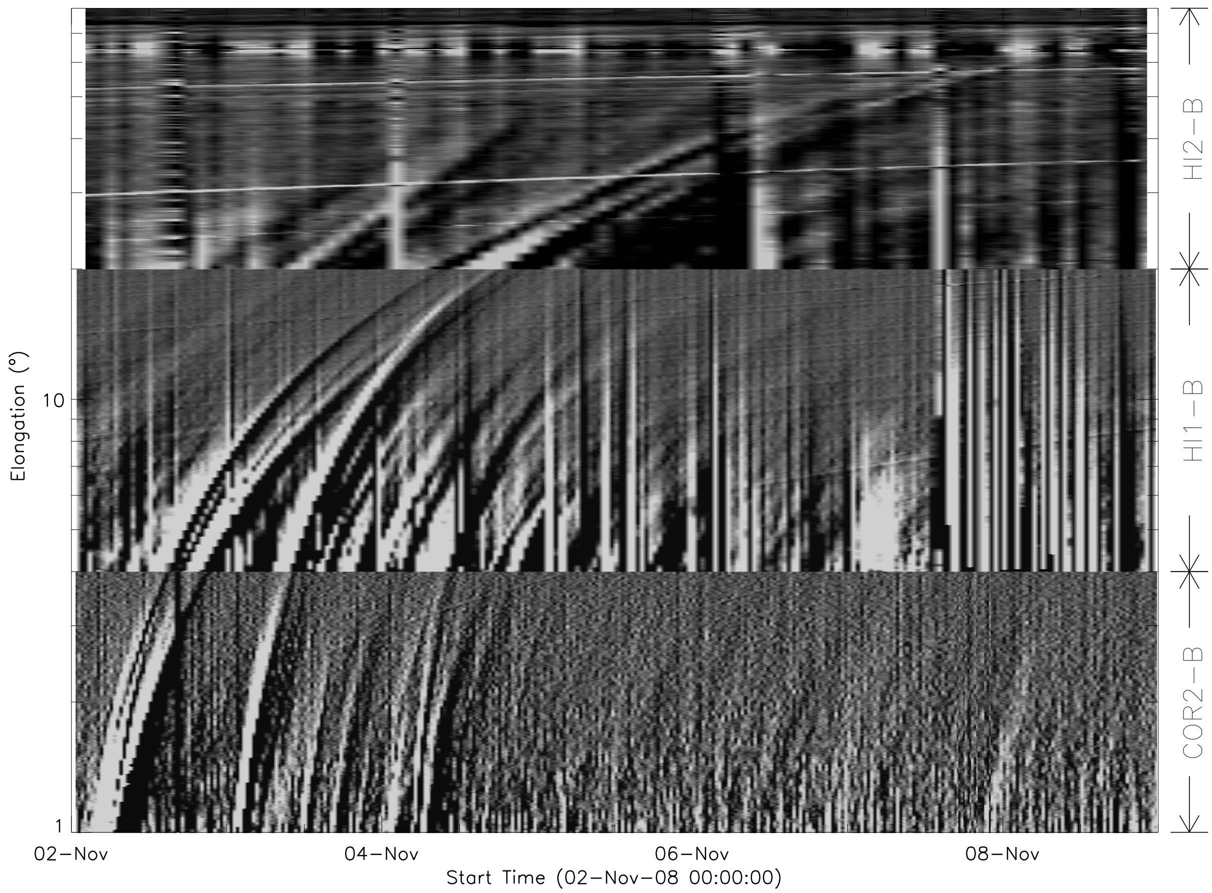

Figure 1: J-map without any legends and decorations for the clarity of Figure 3 in the main text.

1 J-map without any legends and decorations

For clarity, an undecorated J-map is presented as Figure 1. One can compare it with Figure 3 in the main text to recognize the tracks of the two CMEs and their collision signature.

2 Results of GCS Modeling

Figure 2 shows the good match of the GCS modeled flux rope to the observed CMEs. CME1 showed a partial-halo shape inclining to the east from the angle of view of STEREO-A, and looked like a cone towards the west from the angles of views of STEREO-B and the SOlar and Heliospheric Observatory (SOHO)[1], which suggest that CME1 located between STEREO-A and the Earth and was closer to the Sun-STEREO-A line. CME2 looked partial halo with a little inclination to the west from the angle of view of SOHO, but narrow from the angles of views of both STEREO-A and B, which suggest that CME2 also located between STEREO-A and the Earth and was closer to the Sun-Earth line. The CME projections on the plane of sky obviously indicate that CME1 almost propagated along the ecliptic plane but CME2 propagated along the higher latitude. Obviously, based on the projected images on the plane of sky, the latitude of a CME direction could be determined accurately, but the longitude might suffer from a large uncertainty. The uncertainty in longitude, however, could be efficiently reduced by stereoscopic observations. The previous studies have shown that based on STEREO observations the error of the GCS fitting results in latitude is about 2° and that in longitude is 5° on average[2]. In our study, the uncertainty in latitude is simply chosen as 2°, and the uncertainty in longitude is chosen as 10°, 2 times of the average uncertainty in longitude (another reason why we choose a 10° uncertainty is given in the next section). Then we get that the propagation direction of CME1 was $6^\circ \pm 2^\circ$ in latitude and $28^\circ \pm 10^\circ$ in longitude, and that of CME2 was $16^\circ \pm 2^\circ$ in latitude and $8^\circ \pm 10^\circ$ in longitude, which have been listed in Table 1 in the main text. These results are consistent with the imaging observations, and also agree with the results by Kilpua *et al.*[3]. Figure 1 in the main text is plotted based on these

Table 1: Longitudes of the two CMEs derived by different methods

Methods	CME1	CME2
GCS	28	8
Fixed-ϕ	26	14
Harmonic-mean	17	-12
Triangulation	13	1

results.

3 Validating the longitudes of the CMEs

Except GCS model, there are, for example, other three methods that are often used to infer the CME longitude, the Fixed-ϕ method[4,5], the Harmonic-mean method[6], and the Triangulation method[7]. The Fixed-ϕ method assumes that the CME is a compact object (i.e., a single point) and moves along a fixed radial direction with a constant velocity. The Harmonic-mean method assumes that the CME is a sphere with the center of the Sun fixed on the sphere and the center of the sphere propagates along a fixed radial direction with a constant velocity. Both of the methods are based only on the data from a single spacecraft, and infer the CME direction by fitting the track in the J-map. The Triangulation method uses simultaneous observations from two spacecraft, and assumes that the CME tracks recorded in the J-maps from different angles of view correspond to generally the same part of the CME. A summary of these techniques, their advantages and disadvantages can be found in the previous studies[8,9].

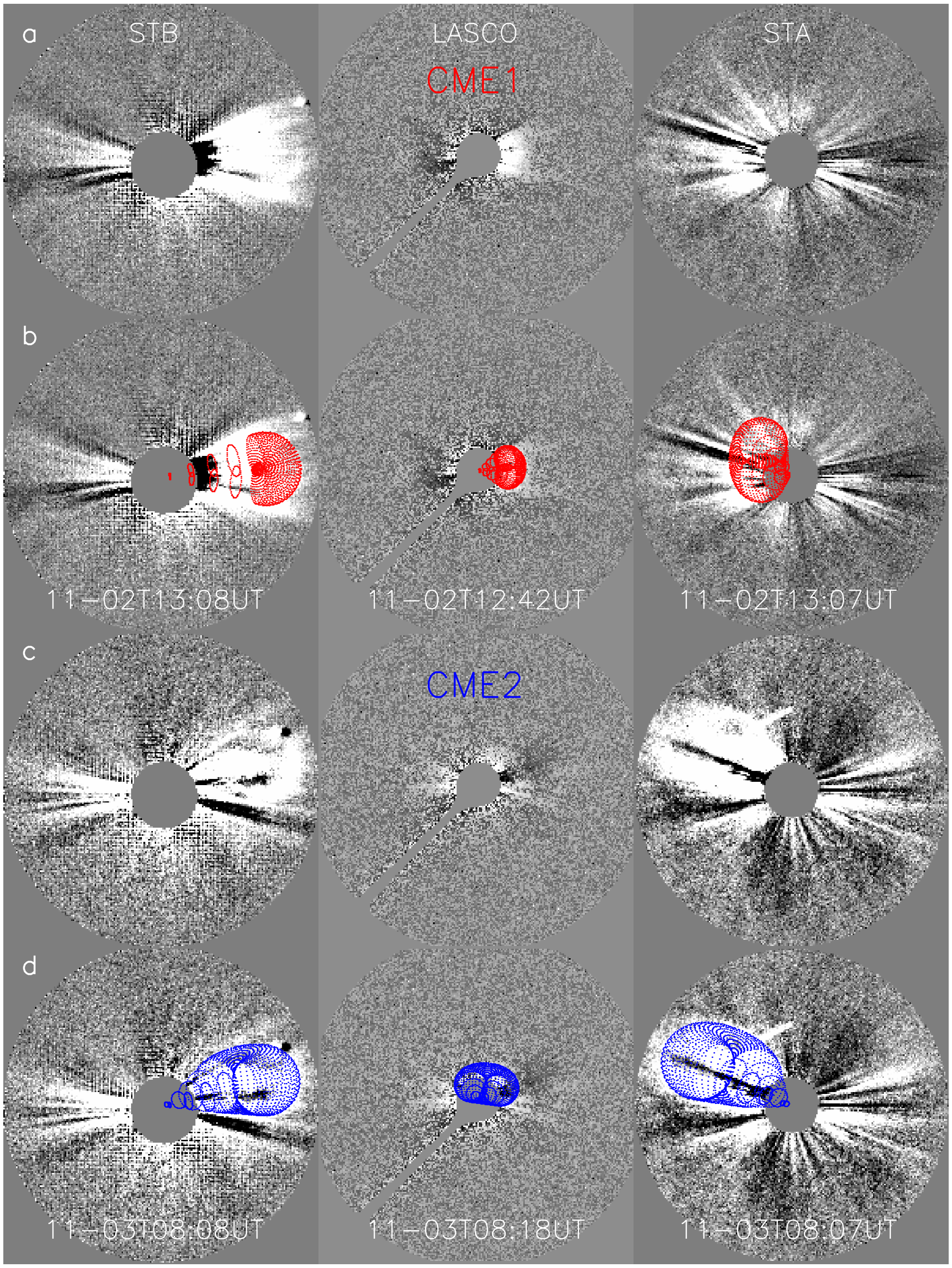

Figure 2: Comparison between the GCS modeled flux rope to the observed CMEs. (a) shows the base-difference images for CME1 from STEREO-B (left), SOHO (middle) and STEREO-A (right). (b) shows the same images with modeled flux rope (red meshes) superimposed on. (c) and (d) are for CME2.

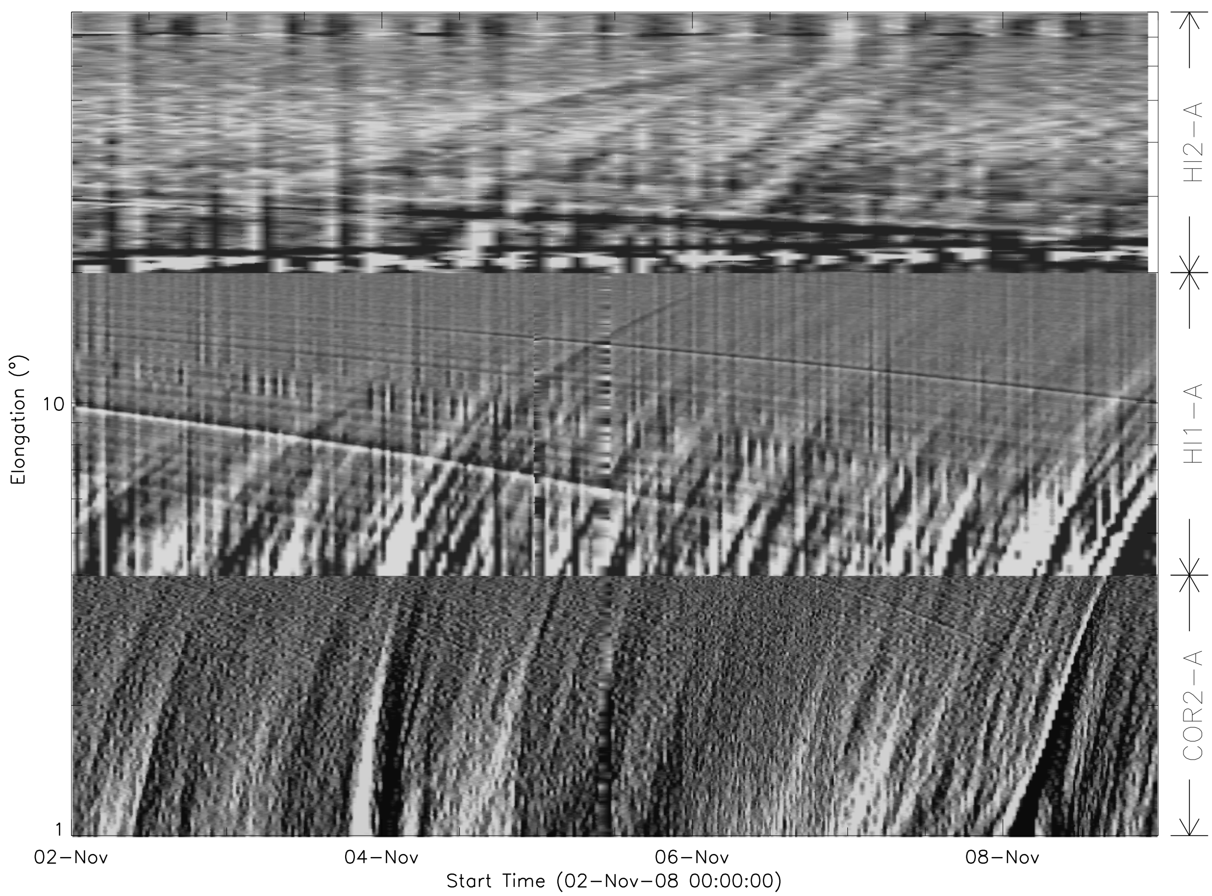

Figure 3: J-map constructed based on the running-difference images from STEREO-A.

Figure 3 shows the J-map generated from the data of STEREO-A for the two CMEs. Table 1 lists the results of the three methods applied to the two CMEs of interest. As a comparison, the GCS model result is also listed. For CME1, the longitudes from GCS model and Fixed-ϕ method are quite close, but the longitude given by the Harmonic-mean method is about 10° smaller and the Triangulation method gives an even smaller value. The imaging observations shown in Figure 2 have suggested that CME1 looks like a limb event in STEREO-B and SOHO, but a partial halo in STEREO-A, which implies a significant deviation from the Sun-Earth line. Thus for this CME, the Harmonic-mean and Triangulation method do not give a reasonable result. For CME2, the results from the four methods are all different. The Harmonic-mean method gives a negative value, which means that the direction of the CME is between the Sun-Earth line and the Sun-STEREO-B line. This is obviously contrary to the observations shown in Figure 2, which suggest that CME2 propagated almost along the Sun-Earth line, because the CME looks symmetrical in the FOVs of STEREO-A and STEREO-B, and slightly deviated toward west in the FOV of SOHO. The longitudes from the other three methods are all possible. Thus we choose the longitude of 8° given by the GCS model, and consider an uncertainty of 10° to cover all the possibilities.

4 Convert elongation angle to heliocentric distance

Figure 4a shows the cross-section of the CME in the ecliptic plane, which illustrates the geometric relationship between the elongation angle and heliocentric distance. It is easy to derive that the heliocentric distance, d_p, of the center of the cross-section and its radius, r_p, can be given by

$$\begin{cases} d_p = \frac{\sin\varepsilon_F + \sin\varepsilon_R}{\sin(\varepsilon_F+\varphi)+\sin(\varepsilon_R+\varphi)} l \\ r_p = \frac{\sin\varepsilon_F \sin(\varepsilon_R+\varphi) - \sin\varepsilon_R \sin(\varepsilon_F+\varphi)}{\sin(\varepsilon_F+\varphi)+\sin(\varepsilon_R+\varphi)} l \end{cases} \tag{1}$$

where ε_F and ε_R are the elongation angle of the measured front and rear edges of the CME in the ecliptic plane, respectively, φ is the longitude of the CME center with respect to the Sun-Observer line, and l is the heliocentric distance of the observer, i.e., STEREO-B. The set of equations is the same as that in the paper by Lugaz *et al.*[10], though they look different. Further, the heliocentric distance. d, of the CME center and the real radius, r, of the CME are given by (as seen in Fig.4b)

$$\begin{cases} d = \frac{d_p}{\cos\theta} \\ r = \sqrt{r_p^2 + d_p^2 \tan^2\theta} \end{cases} \tag{2}$$

where θ is the latitude of the CME center.

5 Validity of the assumption of a sphere

In our analysis, the assumption of a spherical CME plays a key role. However, many previous studies revealed that, due to the stretching of ambient solar wind, a CME will be deformed during its propagation in interplanetary space even if it was initially spherical[11–15]. Such a stretching effect usually gets more and more significant when the CME moves away from the Sun. Thus to check how reasonable the spherical assumption is, we plot the outline of the CME sphere derived from the tracks in the J-map on the HI1 images as indicated by the red (for CME1) and yellow (for CME2) circles shown in Figure 5. It is obvious that even in the FOV of HI1 the red circle matches the outline of CME1 fairly well, which justifies the spherical assumption for CME1. However for

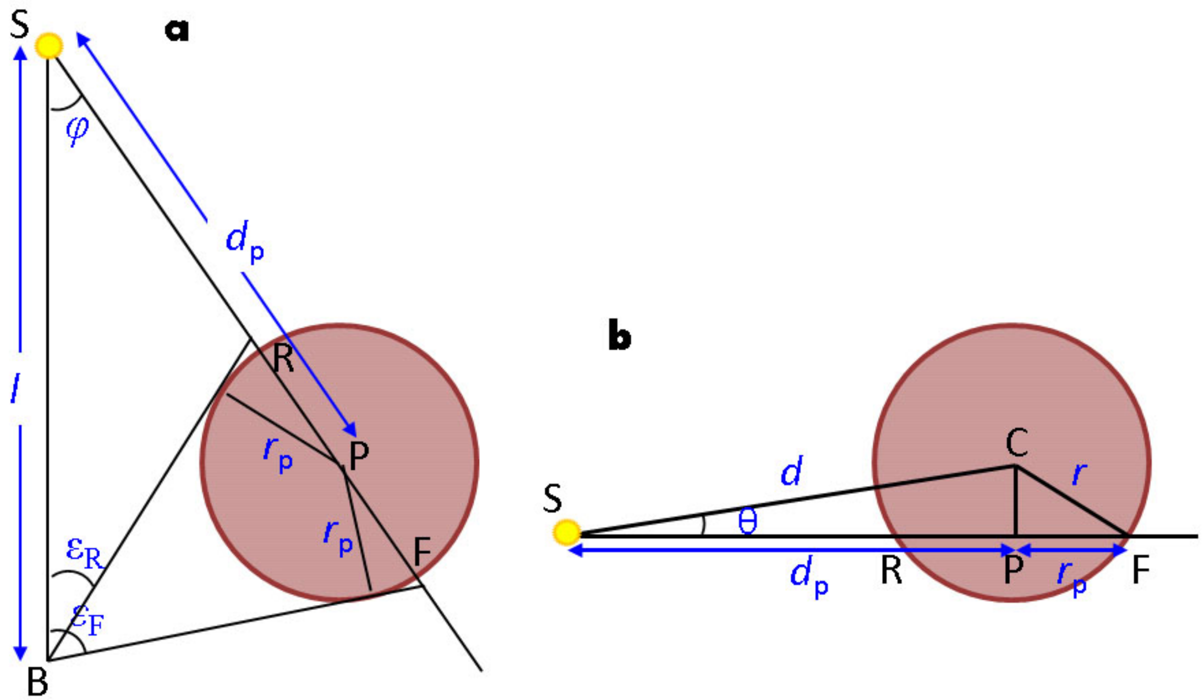

Figure 4: The sketch plot illustrates relationship between the heliocentric distance and elongation angle. (a) presents the ecliptic plane and (b) is the plane perpendicular to the ecliptic plane.

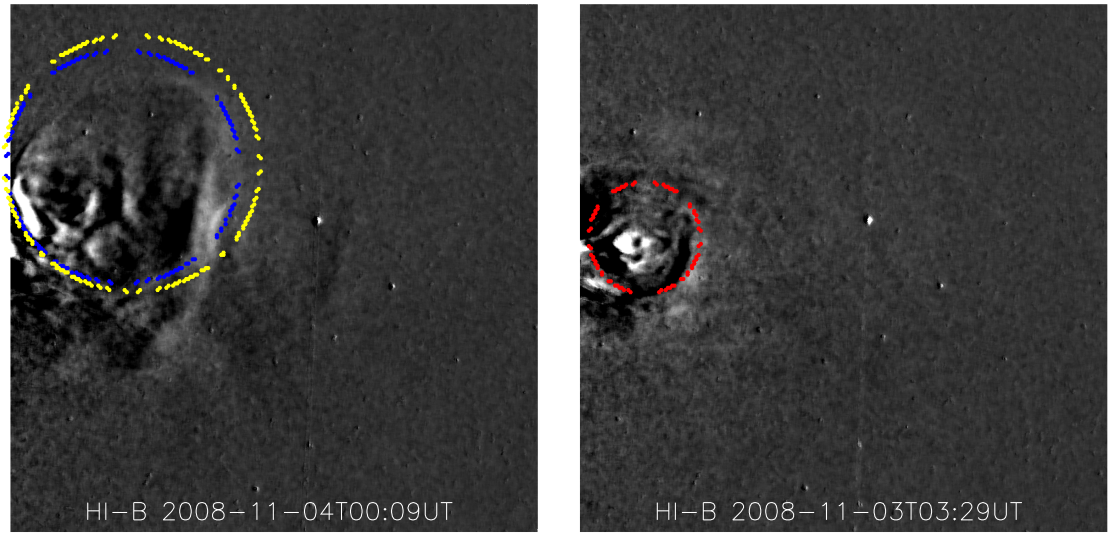

Figure 5: Running-difference images from HI1-B for CME1 (right panel) and CME2 (left panel), respectively.

CME2, there is a significant deviation of the CME shape from a sphere. If we discard the spherical assumption, the collision process will be much more intricate and unsolvable analytically. Thus what we did is to reduce the deviation by changing the size of the sphere to most match the observed CME shape.

The left image in Figure 5 suggests that the rear edge of CME2 is consistent with the observations, but the front edge is obviously overestimated by a factor of about 1.05. After this correction, the CME sphere is indicated by the blue circle in the image, which is closer to the observed morphology. From the J-map, v_{c0} and v_{e0} are derived as 419 and 86 km s^{-1}, respectively, under the assumption of a sphere. Therefore the corrected speeds are $v_c = 407$ km s^{-1} and $v_e = 74$ km s^{-1}.

6 In situ observations of CME1 at 1 AU

By searching all the in situ data at 1 AU (including STEREO-A and B and Wind spacecraft), we do find one and only one CME structure during the period of interest, which was recorded by STEREO-A (Fig.6) and corresponding to CME1. It started at 02:30 UT on 7 November 2008 and ended at 00:40 UT on the next day, as indicated by the shadow. In this region, all the signatures of a typical magnetic cloud (MC)[16] are evident, including the enhanced magnetic field, long and smooth rotation of magnetic vector, low proton temperature and the presence of bidirectional supratheramal electron beams[16,17]. The MC shows an obvious expansion velocity profile. The central speed of the MC is about 342 km s^{-1}, and the expansion speed read from the slope of the velocity profile is about 30 km s^{-1}. The MC appears to propagate in the back of a faster stream with a speed around 380 km s^{-1}.

7 Resolution of velocity vectors for the analysis of collision

Figure 7a shows the coordinates, in which we resolve the velocity vectors and analyze the momentum exchange during the collision. The momentum exchange occurs along the collision direction, defined by the line connecting the centers of the two CMEs (as indicated by the green dashed line). In the heliocentric coordinates (x, y, z), the latitude and longitude of the collision direction are θ_C and φ_C, respectively. We rotate the coordinate system around z-axis to a new one (X, Y, z) so that the collision direction is parallel to the plane of (Y, z). In the new coordinates, the CME velocity $\mathbf{v} = \mathbf{v}_p + \mathbf{v}_z$, where $\mathbf{v}_p$ is the CME propagation speed projected on the ecliptic plane, i.e., the plane

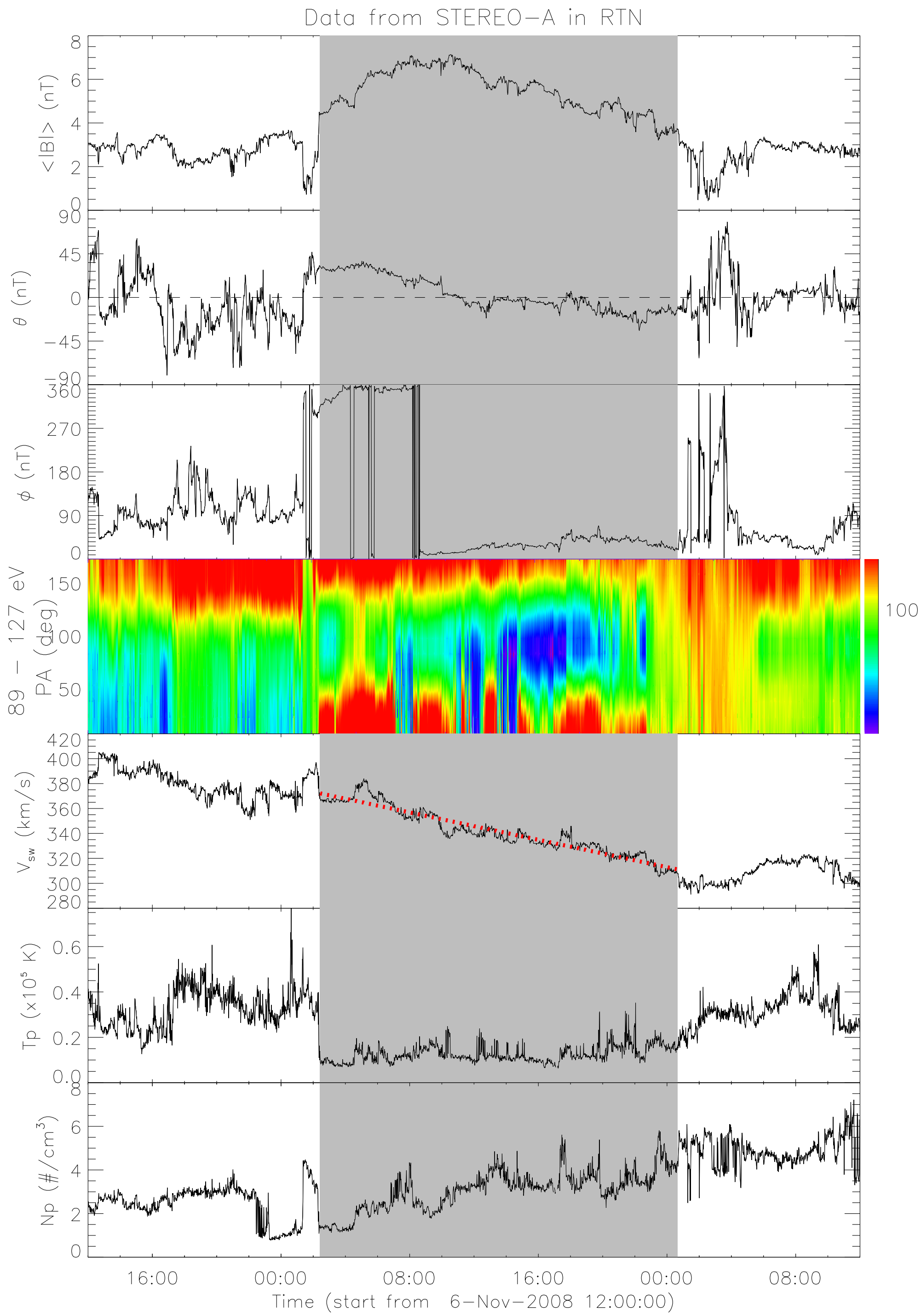

Figure 6: In situ data from STEREO-A. From top to bottom, the panels are the magnetic field strength, the elevation and azimuthal angles of magnetic field vector, pitch angle distribution of 89 – 127 eV electrons in the solar wind frame, the bulk velocity of the solar wind, the proton temperature and number density, respectively.

of (X, Y). Since the CME propagated radially,

$$\begin{cases} v_p = v\cos\theta \\ v_z = v\sin\theta \end{cases} \tag{3}$$

where θ is the latitude of the CME center. Further, $\mathbf{v}_p = \mathbf{v}_X + \mathbf{v}_Y$. $\mathbf{v}_X$ is a vector perpendicular to the collision direction, whose value is given by

$$v_X = v_p \sin(\varphi_C - \varphi) \tag{4}$$

$\mathbf{v}_Y$ and $\mathbf{v}_z$ both have the component along the collision direction. By using $\|$ and $\perp$ for parallel and perpendicular components respectively, we can write $\mathbf{v}_Y = \mathbf{v}_{Y\|} + \mathbf{v}_{Y\perp}$ and $\mathbf{v}_z = \mathbf{v}_{z\|} + \mathbf{v}_{z\perp}$, and the values of them are

$$\begin{cases} v_{Y\|} = v_p \cos(\varphi_C - \varphi)\cos\theta_C \\ v_{Y\perp} = -v_p \cos(\varphi_C - \varphi)\sin\theta_C \\ v_{z\|} = v_z \sin\theta_C \\ v_{z\perp} = v_z \cos\theta_C \end{cases} \tag{5}$$

Finally, we can get the velocity components parallel and perpendicular to the collision direction

$$\begin{cases} v_{\|} = v_{Y\|} + v_{z\|} \\ v_{\perp} = \sqrt{v_X^2 + (v_{Y\perp} + v_{z\perp})^2} \end{cases} \tag{6}$$

The change of the value of $v_{\|}$ will be solved by momentum conservation with a given coefficient of restitution e, while the value of $v_{\perp}$ will remain unchanged during the collision.

Similarly, After the collision (refer to Fig.7b), we have

$$\begin{cases} v'_X = v_X \\ v'_Y = v'_{\parallel}\cos\theta_C - (v_{Y\perp} + v_{z\perp})\sin\theta_C \\ v'_z = v'_{\parallel}\sin\theta_C + (v_{Y\perp} + v_{z\perp})\cos\theta_C \end{cases} \tag{7}$$

and then

$$\begin{cases} v'_p = \sqrt{v'^2_X + v'^2_Y} \\ \varphi' = \arctan\frac{v'_Y}{v'_X} - (\frac{\pi}{2} - \varphi_C) \\ \theta' = \arctan\frac{v'_z}{v'_p} \end{cases} \tag{8}$$

8 The direction change of the CMEs during the collision

In our analysis, we did not consider the change of the parameters of the CMEs during the collision. Among all the parameters, the CME longitude is the most important, as it affects the derived heliocentric distance and the velocity from the J-map. In our calculation, we simply assume that the CME parameters changed in the middle of the collision. The influence of this treatment can be evaluated by analyzing Figure 8. In the figure, the vertical lines T1 and T2 denote the beginning and end of the collision. Consider two extreme cases, one is that the CME parameters changed immediately at the beginning of the collision as indicated by the line OP, and the other is that the CME parameters changed at the end of the collision as indicated by the line QN. The actual process should be bounded by OP and QN. For CME1, $v_c = 243$ km s^{-1}, $\theta = 6°$, $\varphi = 68°$ (including the angle $40°$ between the STEREO-B and the Earth), $\Delta\varphi_v = 7°$ (c.f. Table 1 in the main text). Since the collision lasted about 16 hours, it is derived that the length of the line OQ is about 0.093

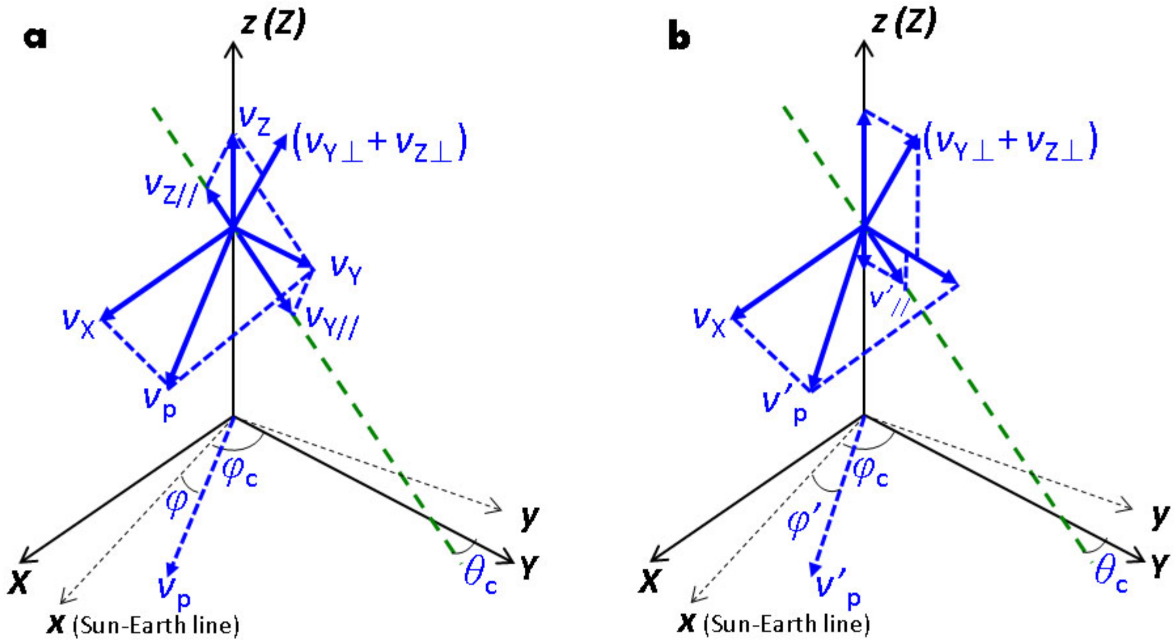

Figure 7: Resolution of velocity vectors. The plane of (x, y) is the ecliptic plane. (a) illustrates how to resolve a velocity vector into the components parallel and perpendicular to the collision direction, and (b) illustrates how to compose the parallel and perpendicular components back into the velocity vector after the collision.

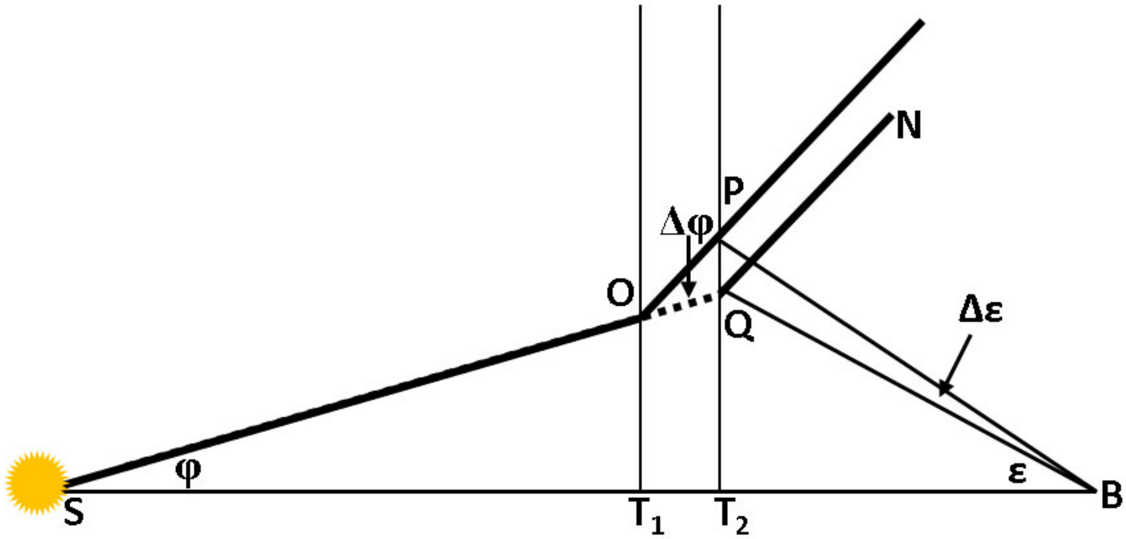

Figure 8: Sketch illustrating the influence of the direction change of the CMEs during the collision. The thick lines indicate the trajectory of a CME in the ecliptic plane.

AU, and the length of the line PQ is about 0.044 AU. The heliocentric distance of STEREO-B is about 1.07 AU, and the elongation angle of CME1 as seen from STEREO-B after the collision is about 22° (i.e., ε in Figure 8), and therefore the length of the line BT_2 is about 0.868 AU and the length of the line QT_2 is about 0.351 AU. Then we can infer that $\Delta\varepsilon = 2.5^\circ$ and the uncertainty of our derived elongation angle of CME1 after the collision is less than $0.5\Delta\varepsilon = 1.25^\circ$. This error will cause a slight difference in the predicted track of the front edge of CME1 and therefore the coefficient of restitution e, which is 5.0 for line OP and 6.2 for line QN. This error range is about 0.1 times of that caused by the uncertainties of the CMEs' speeds, and even much smaller than that caused by the uncertainties of the CMEs' longitudes. Thus the influence of the direction change of the CMEs during the collision on our final result is not significant.

9 Influence of mass ratio on the result

To evaluate the influence of mass ratio on our result, we scan the value of mass ratio from 0.5 to 2.0 and calculate the coefficient of restitution e. This treatment is equivalent to assuming the mass uncertainty of CME1 or CME2 exceeds $33 - 67\%$. It is found that the value of e is larger than 3 in this range of mass ratio, Moreover, according to the trend shown in Figure 9, it could be inferred that the collision would remain super-elastic even if the mass ratio approaching zero. We may conclude that the error in the estimation of mass might be large, but will not destroy the main point of the work.

10 Discussion about post-collision phase

In this event, the two CMEs experienced a super-elastic collision, and gained kinetic energy. The analysis suggests that the separating speed (the same meanting as approaching speed) between them is about 172 km s^{-1} larger than the sum of the expansion speeds of them, ~ 117 km s^{-1}. It is therefore expected that the two CMEs will separate after the collision. At that time, the two CMEs were almost running out of the FOV of HI1, and became extremely faint. Thus it is not possible to check in the imaging observations whether or not the two CMEs did eventually separate. However, complex ejecta[18] and multiple-magnetic-cloud (Multi-MC) structures[19,20] are often observed in situ during solar maxima. Such structures are obviously the result of the collision of multiple CMEs. Thus we could carry out a study on the issue in future work to see whether or not the CMEs in complex structures may be separating based on in situ data.

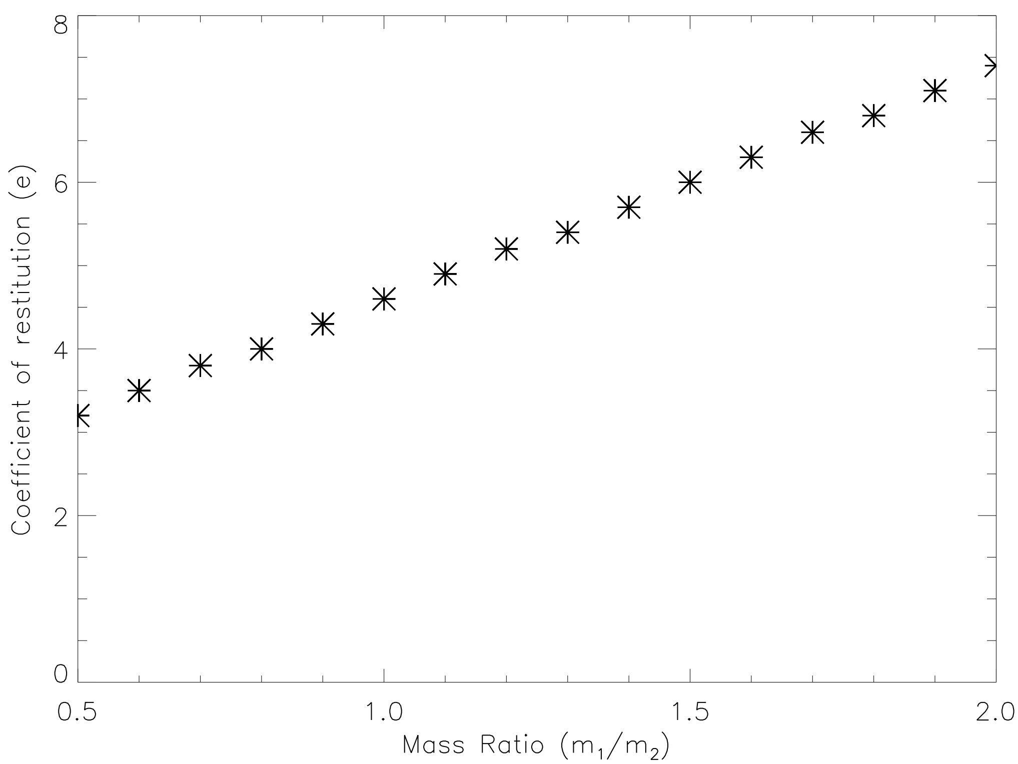

Figure 9: The dependence of the value of the coefficient of restitution on the mass ratio of the two CMEs.

11 Momentum coupling with the solar wind

Except collision with another CME, a CME may also change its speed and direction by interaction with ambient solar wind[21,22]. Since the enhancement of brightness between the two CMEs in the imaging data may be simply due to the superposition of the two CMEs, it is first necessary to check if the kinetic evolution of CME1 track shown in the J-map can be attributed to the interaction with the solar wind without the CME-CME collision. In our analysis, we use a constant propagation speed for CME1 before the 'collision' (we still use the term 'collision' for the time of the brightness enhancement). Actually, CME1 has a very weak acceleration of about 0.5 m s^{-2} derived from the 2nd order fitting. Even if we considered the constant weak acceleration for CME1, the super-elastic collision nature would not be changed. Here we use the drag-force model[21,23,24], which is more realistic, to fit the track of CME1 front edge in the J-map before the 'collision', and extrapolated it to the post-'collision' phase. It is found that the extrapolated curve cannot match the observed track (see Fig.10). Thus, if the two CMEs did not touch each other, it is difficult to explain how the solar wind changed CME1 speed and direction only after the apparent 'collision'.

Further, the efficiency of the CME1 momentum change by the solar wind and that by the collision can be estimated and compared. According to the number listed in Table 1 of the main text, the momentum of CME1 changed 31% by the collision in 16 hours. After the collision, CME1 speed increased to 316 km s^{-1}. The in situ speed of CME1, which is observed after about 64 hours, is about 342 km s^{-1}. Thus, the momentum of CME1 changed 8% by the solar wind in 64 hours after the collision. The efficiency of the solar wind is about 6.5% of that of the collision.

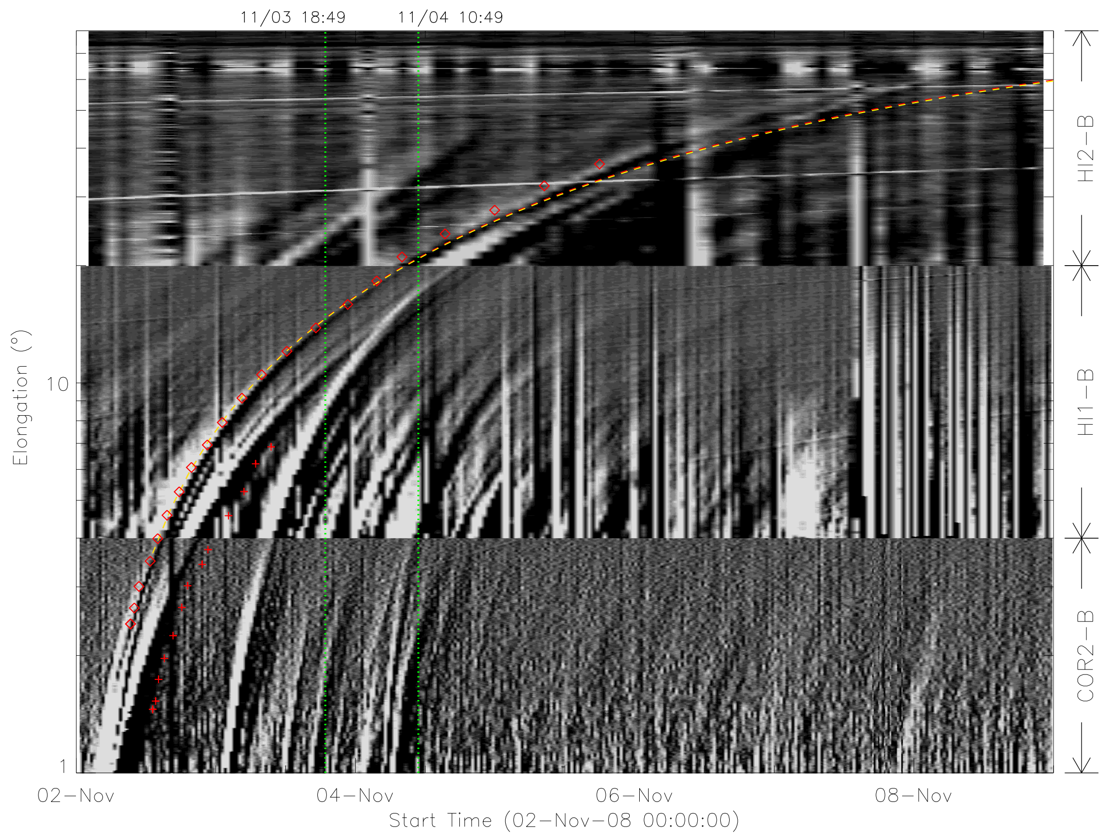

Figure 10: Same as the J-map shown in Figure 3 of the main text, except the red (a constant solar wind speed of 380 km s^{-1} according to the in situ observations is applied in the model) and yellow (a linear increasing solar wind speed from 300 to 380 km s^{-1} is applied) lines are obtained from the drag-force model, in which the CME acceleration by the solar wind is taken into account.

12 Absence of shock ahead of CME2

If CME2 drove a shock, the driven shock will provide the extra momentum exchange to CME1[6]. The resolution of HI1 imaging data is not high enough to distinguish if there was a shock. We then check with the radio data as type II radio bursts are a good indicator for shocks. Figure 11 shows the observations from WIND/WAVES[25] and STEREO/WAVES[26]. It could be found that there are at least four type III radio bursts in all the radio instruments, but no type IIs. Thus no shock signatures could be found in radio observations. Besides, some radio emissions around $100-400$ kHz from 01:00 to 03:00 UT on November 4, which is in the middle of the collision phase, were received by WIND/Waves. However, similar emissions cannot be found at the other two receivers onboard STEREO. Therefore, the radio emissions observed by Wind do not indicate the presence of a shock or the interaction of the two CMEs. It was probably the auroral kilometric radiation (AKR) from the Earth. Although we do not find any signature of shocks, we cannot rule out that CME2 did not drive a shock. But we may be confident that the shock, if any, will be very weak and therefore do not significantly affect our analysis of the two CMEs' collision.

References

1. Domingo, V., Fleck, B. & Poland, A. I. SOHO: The solar and heliospheric observatory. *Space Sci. Rev.* **72**, 81–84 (1995).

2. Thernisien, A., Vourlidas, A. & Howard, R. Forward modeling of coronal mass ejections using STEREO/SECCHI data. *Sol. Phys.* **256**, 111–130 (2009).

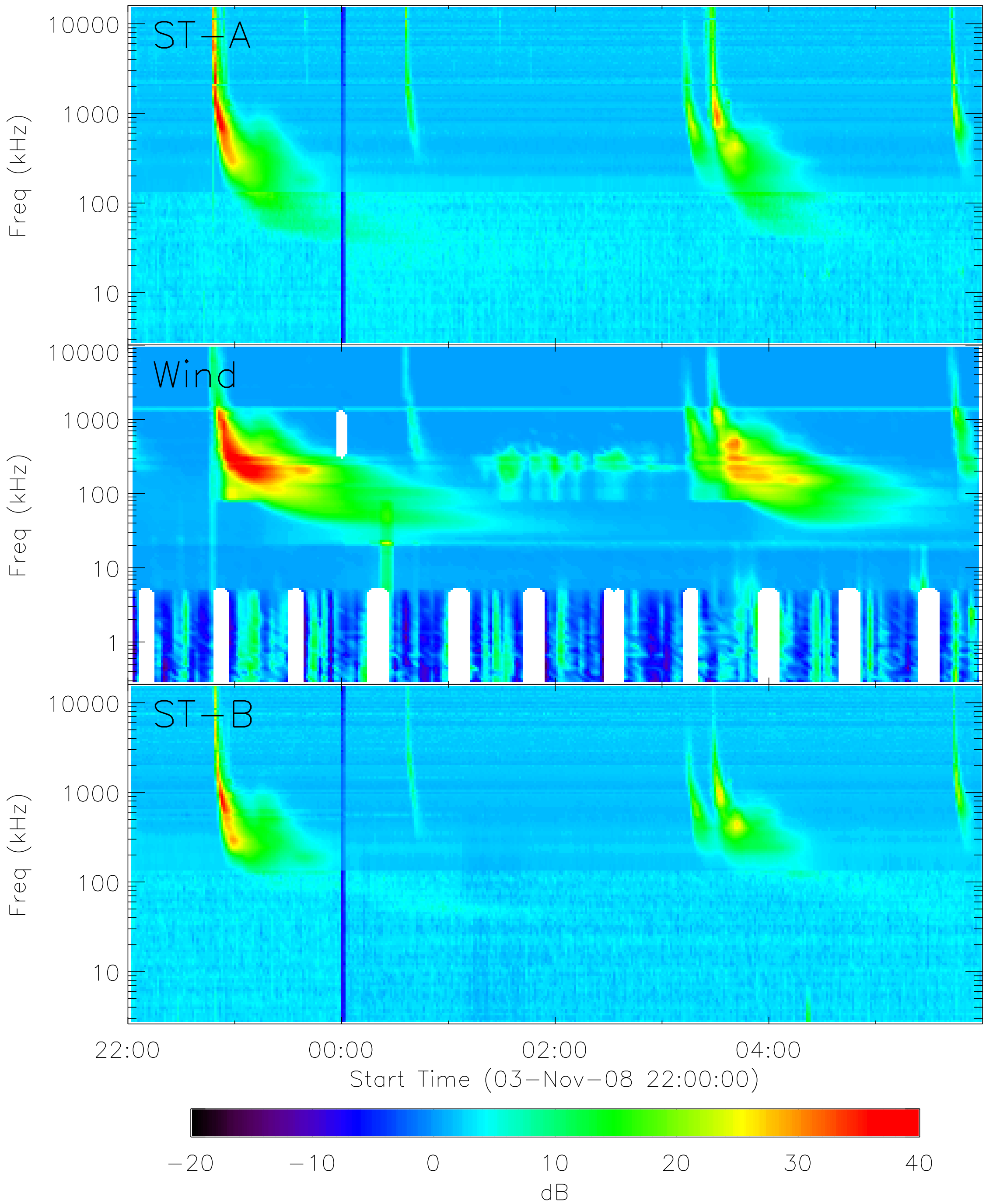

Figure 11: Radio observations from STEREO-A/WAVES (upper), WIND/WAVES (middle) and STEREO-B/WAVES (lower).

3. Kilpua, E. K. J. *et al.* STEREO observations of interplanetary coronal mass ejections and prominence deflection during solar minimum period. *Ann. Geophys.* **27**, 4491–4503 (2009).

4. Sheeley, Jr., N. R., Walters, J. H., Wang, Y.-M. & Howard, R. A. Continuous tracking of coronal outflows: Two kinds of coronal mass ejections. *J. Geophys. Res.* **104**, 24739–24768 (1999).

5. Kahler, S. W. & Webb, D. V arc interplanetary coronal mass ejections observed with the solar mass ejection imager. *J. Geophys. Res.* **112**, A09103 (2007).

6. Lugaz, N., Vourlidas, A. & Roussev, I. I. Deriving the radial distances of wide coronal mass ejections from elongation measurements in the heliosphere application to CME-CME interaction. *Ann. Geophys.* **27**, 3479–3488 (2009).

7. Liu, Y. *et al.* Geometric triangulation of imaging observations to track coronal mass ejections continuously out to 1 AU. *Astrophys. J.* **710**, L82–L87 (2010).

8. Lugaz, N. Accuracy and limitations of fitting and stereoscopic methods to determine the direction of coronal mass ejections from heliospheric imagers observations. *Sol. Phys.* **267**, 411–429 (2010).

9. Liu, Y. *et al.* Reconstructing coronal mass ejections with coordinated imaging and in situ observations: Global structure, kinematics, and implications for space weather forecasting. *Astrophys. J.* **722**, 1762–1777 (2010).

10. Lugaz, N. *et al.* Determining the azimuthal properties of coronal mass ejections from multi-spacecraft remote-sensing observations with STEREO SECCHI. *Astrophys. J.* **715**, 493–499 (2010).

11. Crooker, N. V. & Intriligator, D. S. A magnetic cloud as a distended flux rope occlusion in the heliospheric current sheet. *J. Geophys. Res.* **101**, 24343–24348 (1996).

12. Russell, C. T. & Mulligan, T. The true dimensions of interplanetary coronal mass ejections. *Adv. Space Res.* **29**, 301–306 (2002).

13. Riley, P. *et al.* Using an MHD simulation to interpret the global context of a coronal mass ejection observed by two spacecraft. *J. Geophys. Res.* **108**, 1272 (2003).

14. Riley, P. & Crooker, N. U. Kinematic treatment of coronal mass ejection evolution in the solar wind. *Astrophys. J.* **600**, 1035–1042 (2004).

15. Liu, Y., Richardson, J. D., Belcher, J. W. & Kasper, J. C. Constraints on the global structure of magnetic clouds: Transverse size and curvature. *J. Geophys. Res.* **111**, A12S03 (2006).

16. Burlaga, L., Sittler, E., Mariani, F. & Schwenn, R. Magnetic loop behind an interplanetary shock: Voyager, Helios, and IMP 8 observations. *J. Geophys. Res.* **86**, 6673–6684 (1981).

17. Gosling, J. T. *et al.* Bidirectional solar wind electron heat flux events. *J. Geophys. Res.* **92**, 8519–8535 (1987).

18. Burlaga, L. F., Plunkett, S. P. & St. Cyr, O. C. Successive CMEs and complex ejecta. *J. Geophys. Res.* **107**, 1266 (2002).

19. Wang, Y. M., Wang, S. & Ye, P. Z. Multiple magnetic clouds in interplanetary space. *Sol. Phys.* **211**, 333–344 (2002).

20. Wang, Y. M., Ye, P. Z. & Wang, S. Multiple magnetic clouds: Several examples during March – April, 2001. *J. Geophys. Res.* **108**, 1370 (2003).

21. Cargill, P. J. On the areodynamic drag force acting on interplanetary coronal mass ejections. *Sol. Phys.* **221**, 135–149 (2004).

22. Wang, Y. *et al.* Impact of the major coronal mass ejections on geo-space during September 7 – 13, 2005. *Astrophys. J.* **646**, 625–633 (2006).

23. Vršnak, B. Deceleration of coronal mass ejections. *Sol. Phys.* **202**, 173–189 (2001).

24. Byrne, J. P., Maloney, S. A., Mcateer, R. T. J., Refojo, J. M. & Gallagher, P. T. Propagation of an Earth-directed coronal mass ejection in three dimensions. *Nature Commun.* **1**, 74 (2010).

25. Bougeret, J.-L. *et al.* Waves: The radio and plasma wave investigation on the Wind spacecraft. *Space Sci. Rev.* **71**, 231–263 (1995).

26. Bougeret, J.-L. *et al.* S/WAVES: The radio and plasma wave investigation on the STEREO mission. *Space Sci. Rev.* **136**, 487–528 (2008).

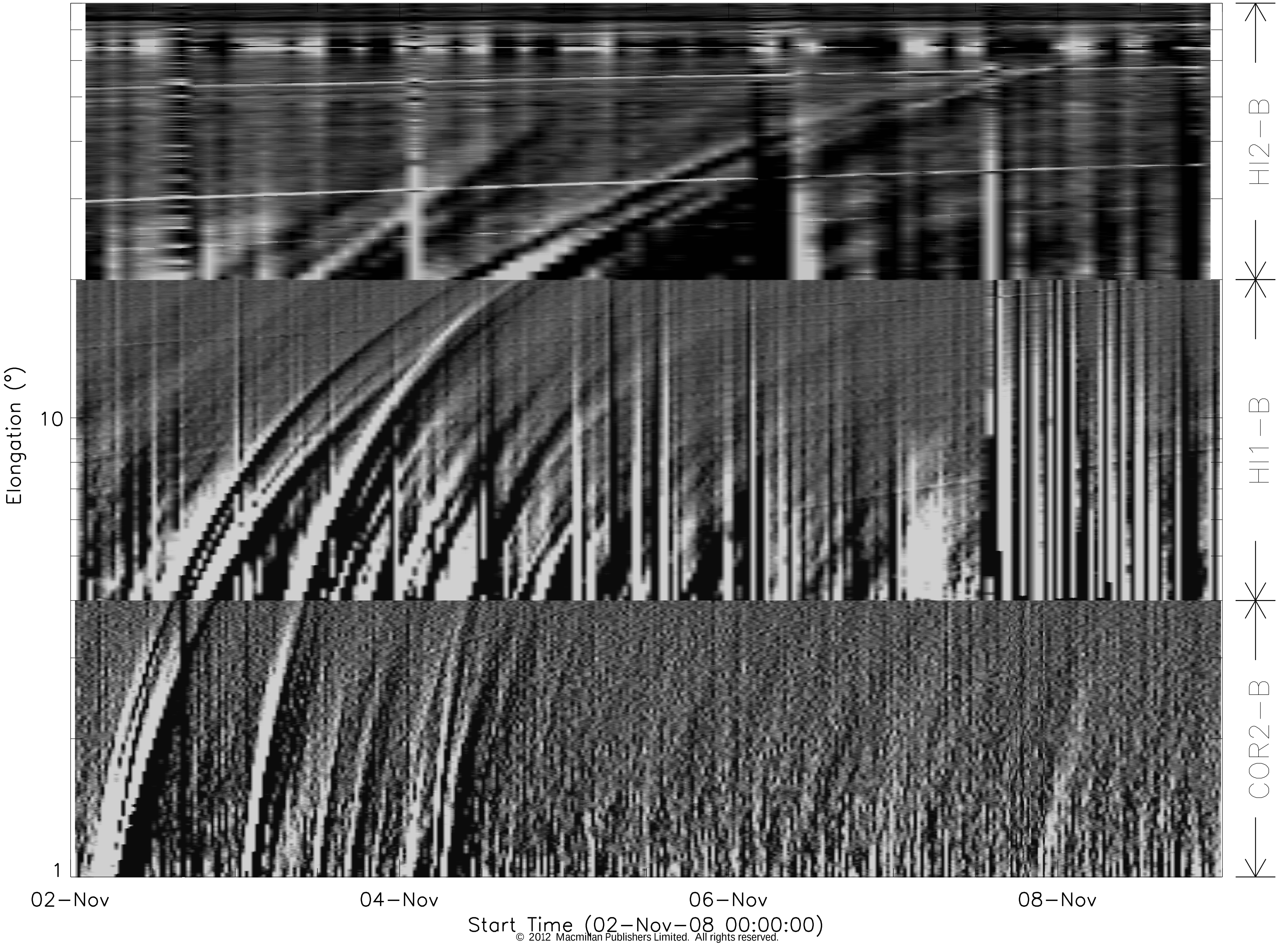

HI2−B
HI1−B
COR2−B
Elongation (°)
10
1
02−Nov
04−Nov
06−Nov
08−Nov
Start Time (02−Nov−08 00:00:00)

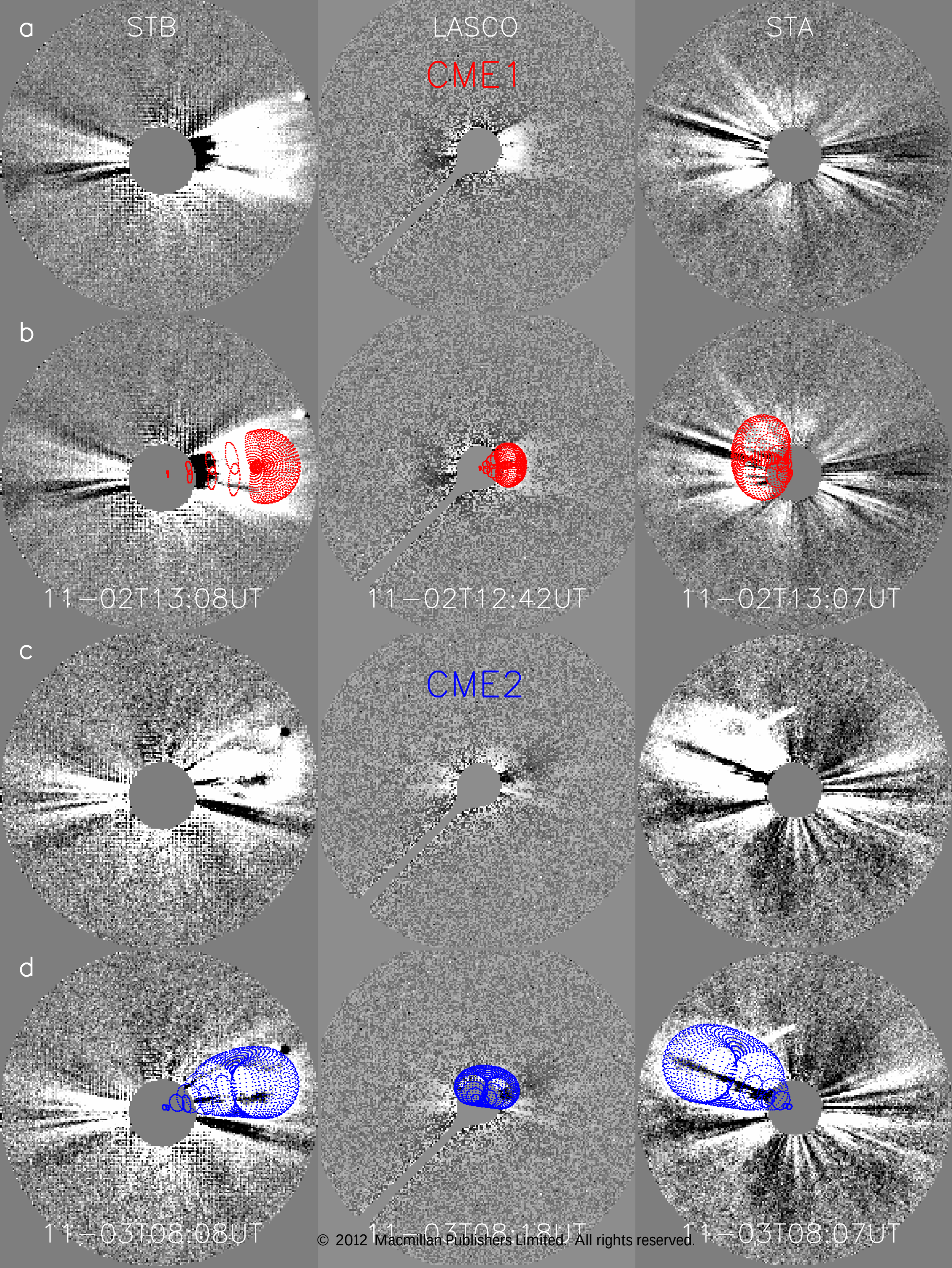
a
STB
LASCO
STA
CME1
b
11-02T13:08UT
11-02T12:42UT
11-02T13:07UT
c
CME2
d
11-03T08:08UT
11-03T08:18UT
11-03T08:07UT

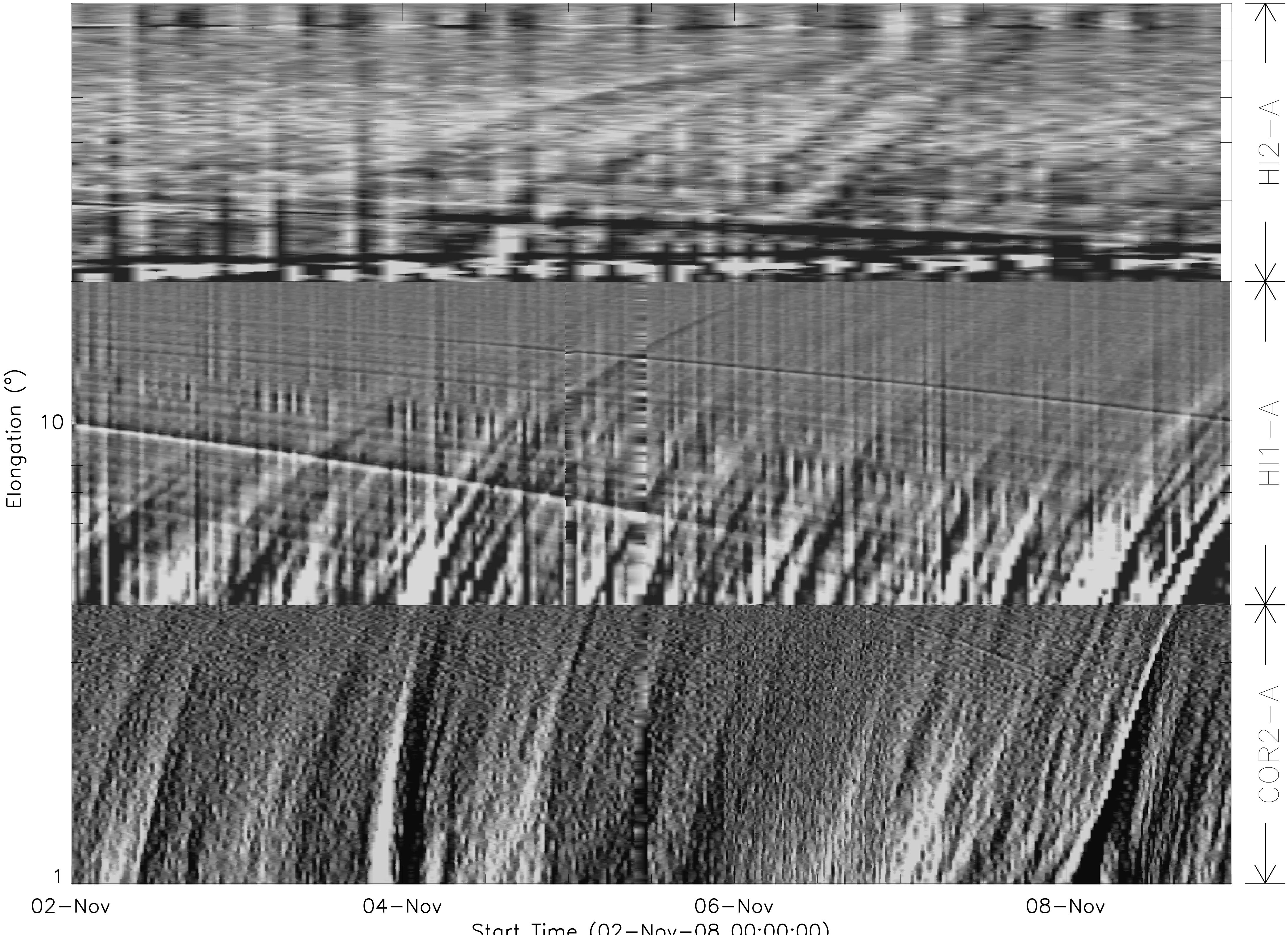

HI2−A
HI1−A
COR2−A
Elongation (°)
10
1
02−Nov
04−Nov
06−Nov
08−Nov
Start Time (02−Nov−08 00:00:00)

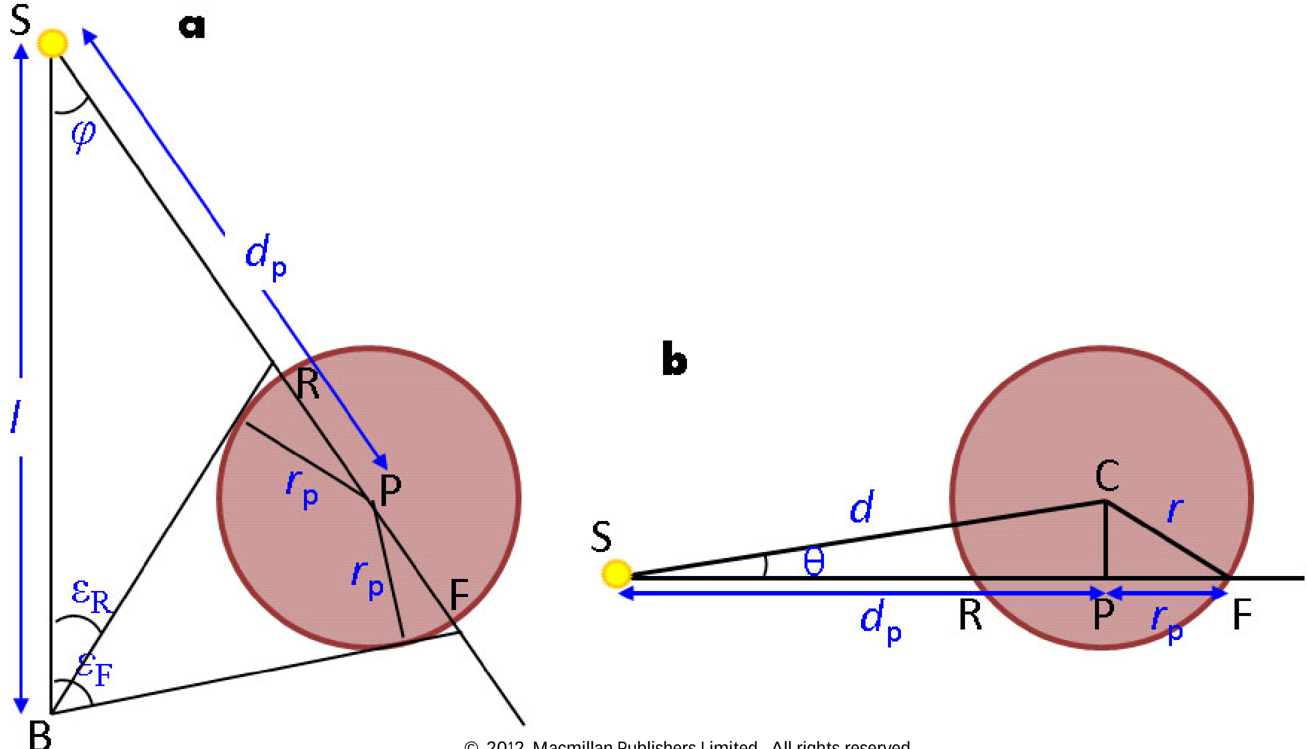
a
S
φ
d_p
l
R
r_p
P
r_p
F
ε_R
ε_F
B
b
S
θ
d
C
r
d_p
R
P
r_p
F

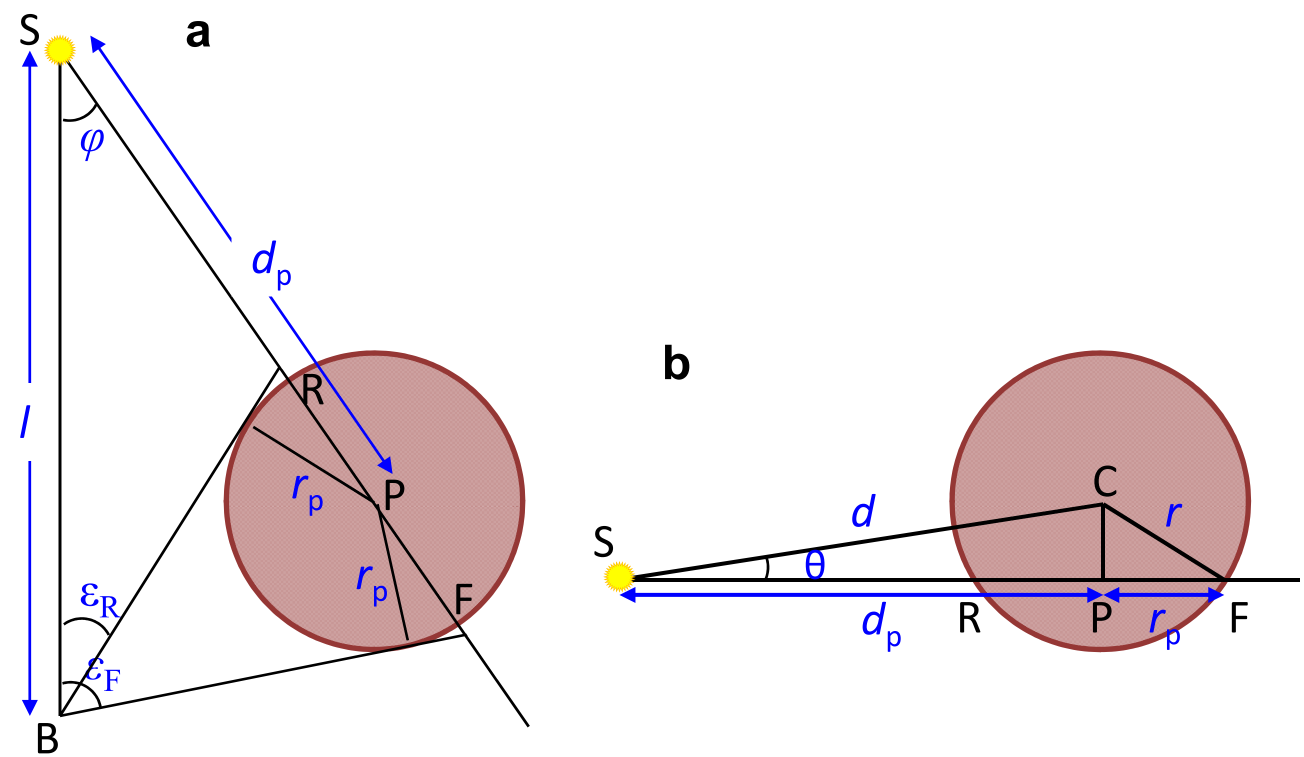
a
S
φ
d_p
R
r_p
P
r_p
F
l
ε_R
ε_F
B
b
C
d
r
S
θ
d_p
R
P
r_p
F

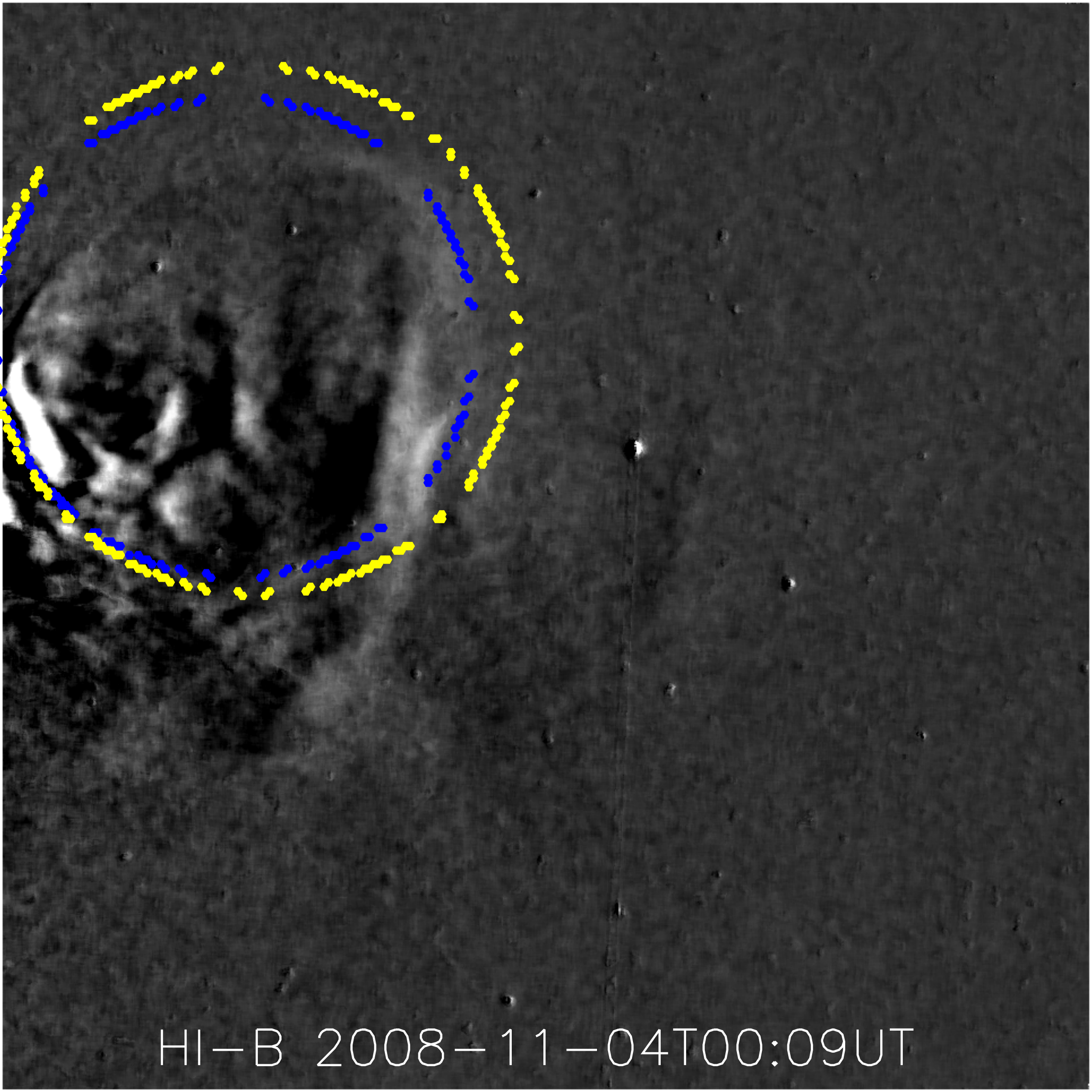
HI-B 2008-11-04T00:09UT

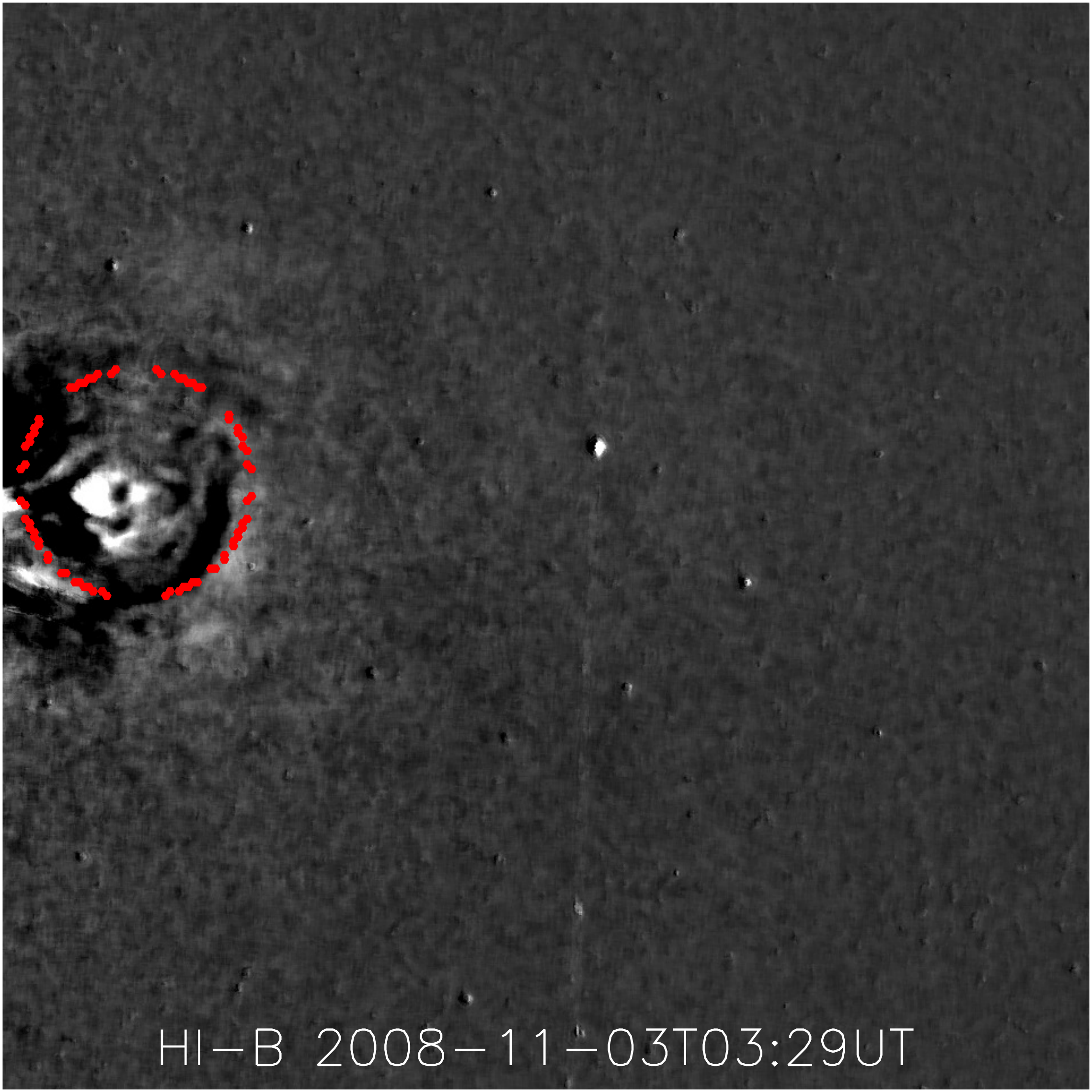
HI-B 2008-11-03T03:29UT

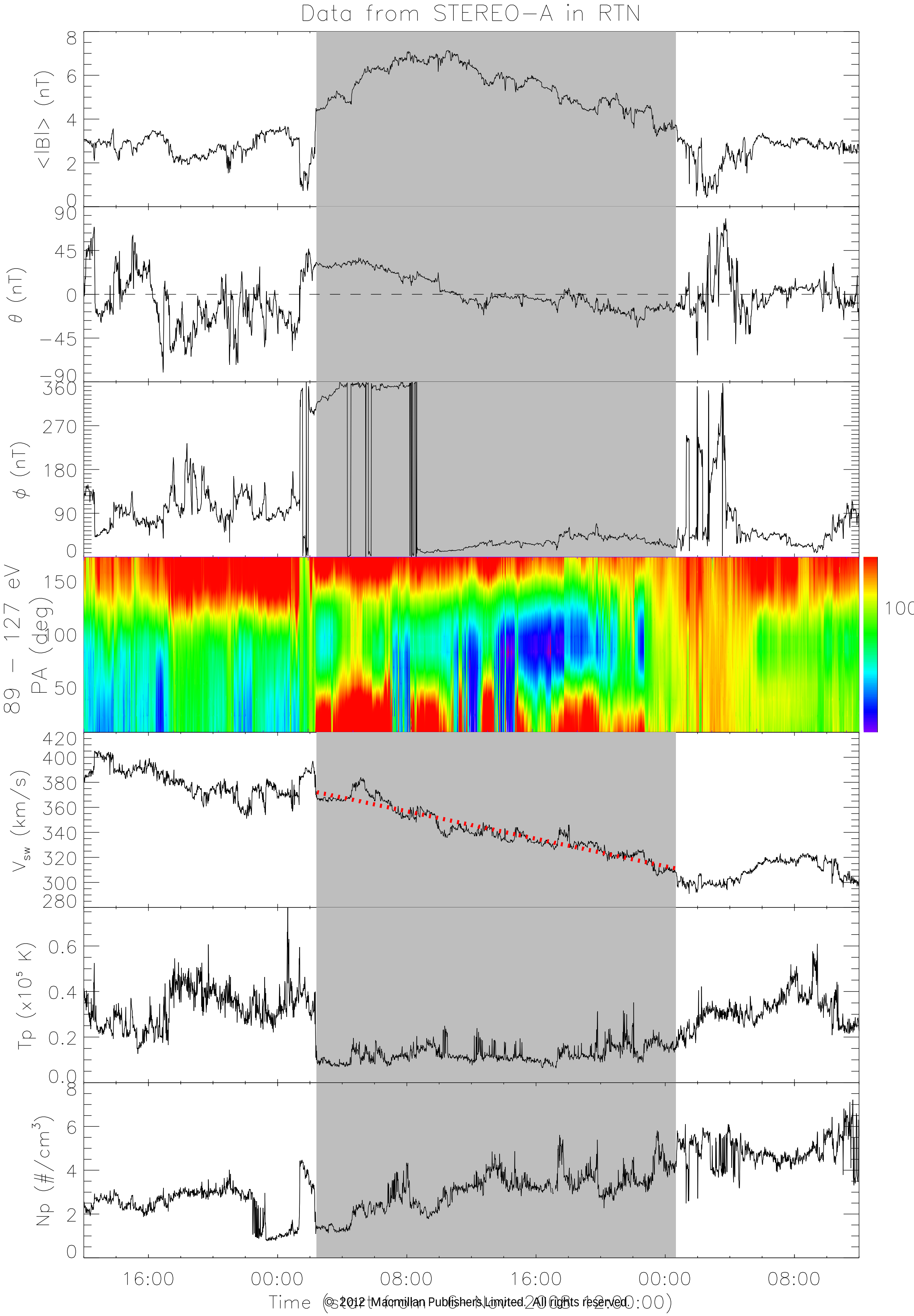
Data from STEREO-A in RTN
<|B|> (nT)
θ (nT)
φ (nT)
89 - 127 eV PA (deg)
100
V_sw (km/s)
Tp (x10^5 K)
Np (#/cm^3)
16:00
00:00
08:00
16:00
00:00
08:00
Time (start from 6 Nov 2008 12:00:00)

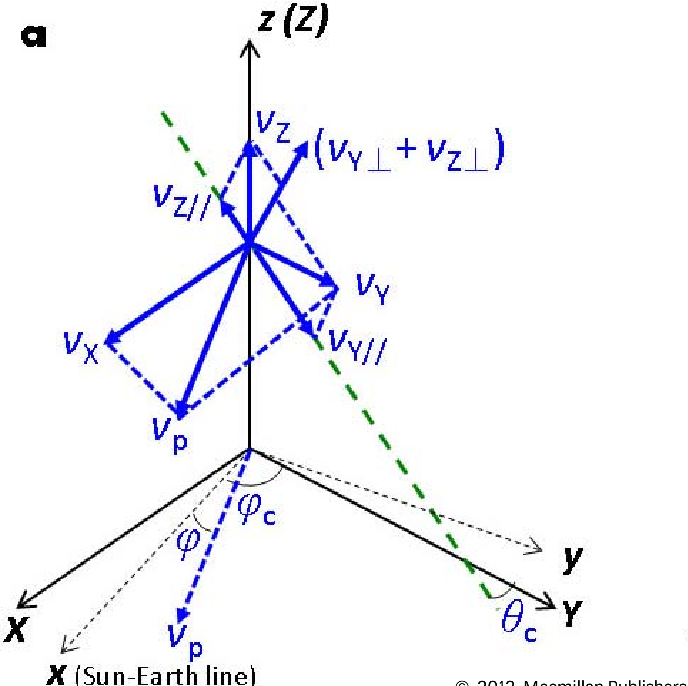
a
b
z (Z)
v_Z
$(v_{Y\perp}+v_{Z\perp})$
$v_{Z//}$
v_Y
v_X
$v_{Y//}$
v_p
$v'_{//}$
v'_p
φ_c
φ
φ'
θ_c
X
Y
y
x (Sun-Earth line)

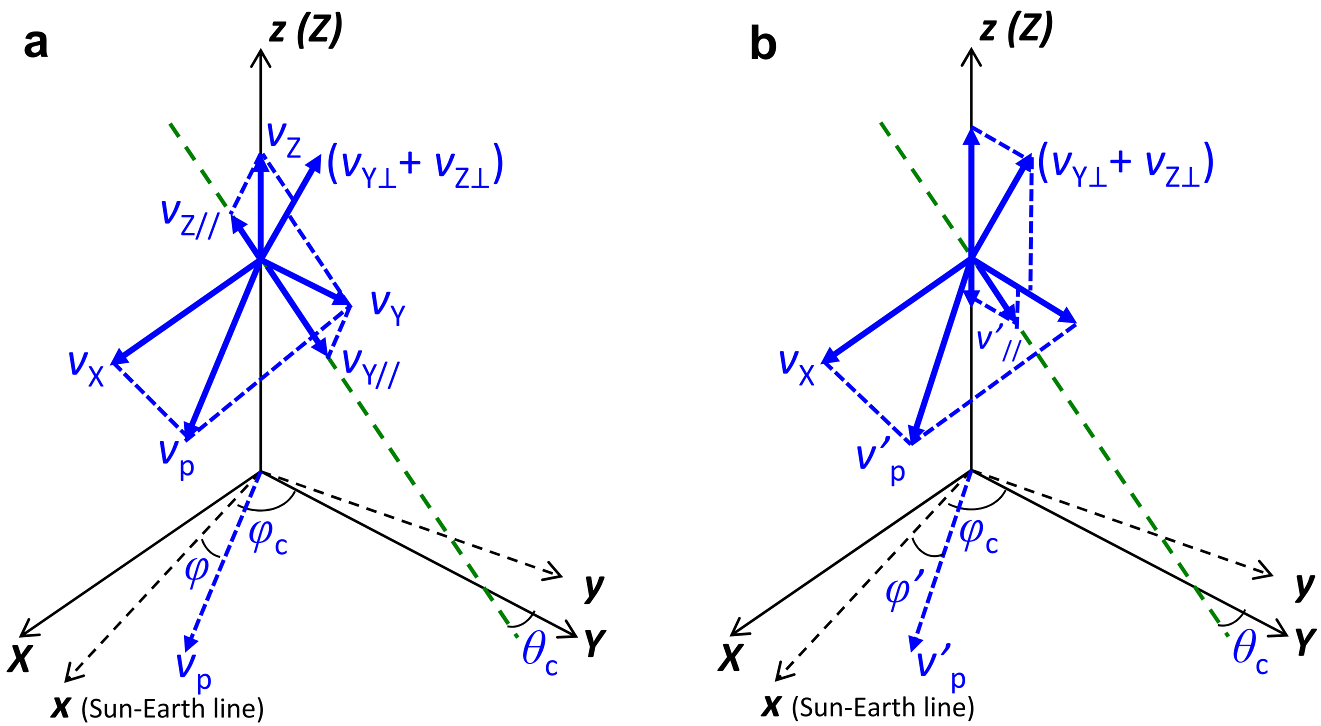
a
z (Z)
v_Z
$(v_{Y\perp} + v_{Z\perp})$
$v_{Z//}$
v_Y
v_X
$v_{Y//}$
v_p
φ_c
φ
y
X
v_p
θ_c
Y
x (Sun-Earth line)
b
z (Z)
$(v_{Y\perp} + v_{Z\perp})$
v_X
$v'_{//}$
v'_p
φ_c
φ'
y
X
v'_p
θ_c
Y
x (Sun-Earth line)

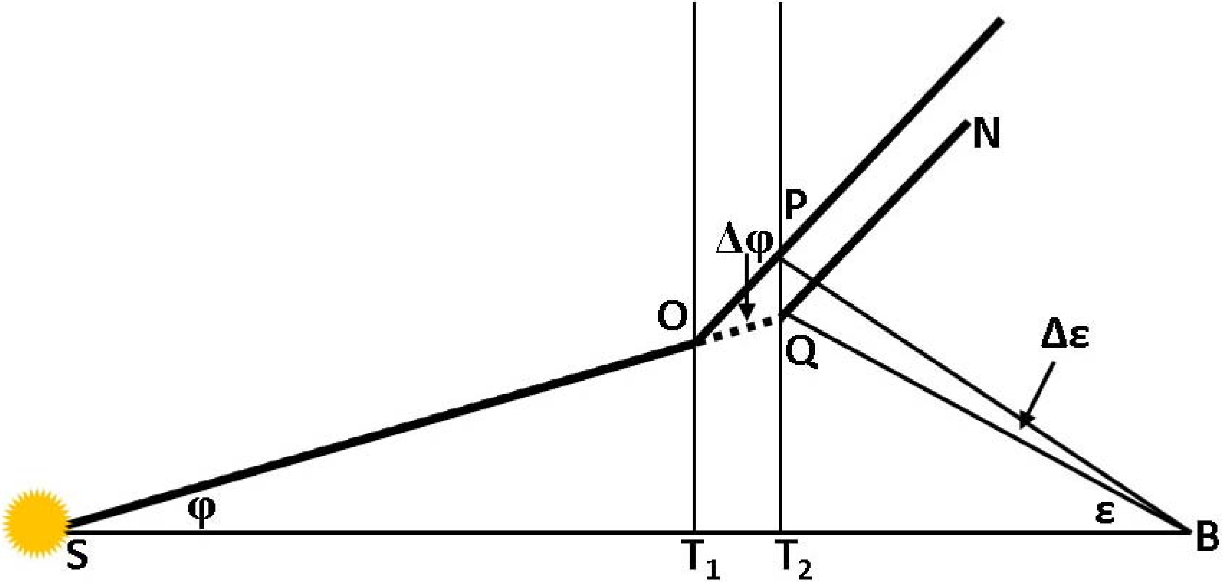

N
P
Δφ
O
Q
Δε
φ
ε
S
T1
T2
B

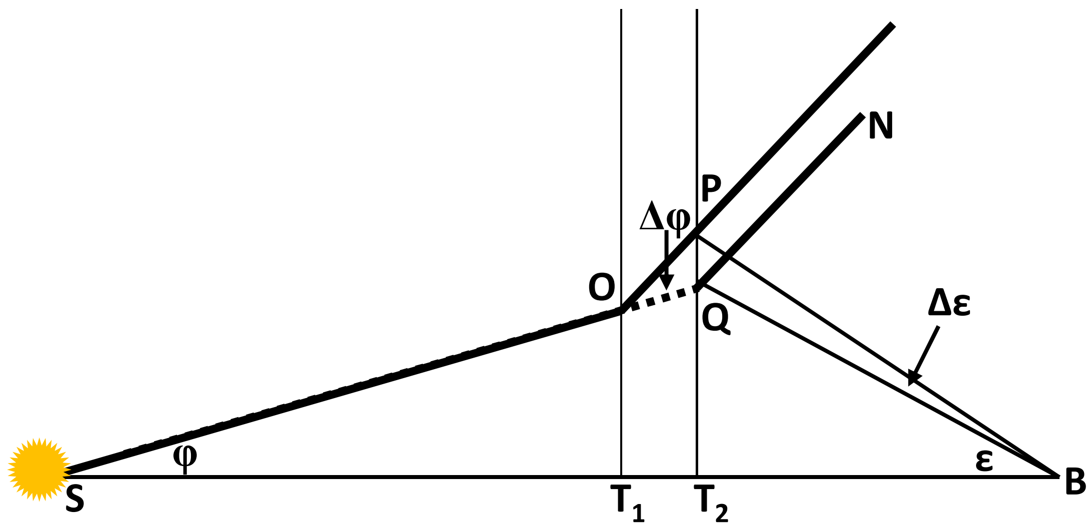
N
P
Δφ
O
Q
Δε
φ
ε
S
T1
T2
B

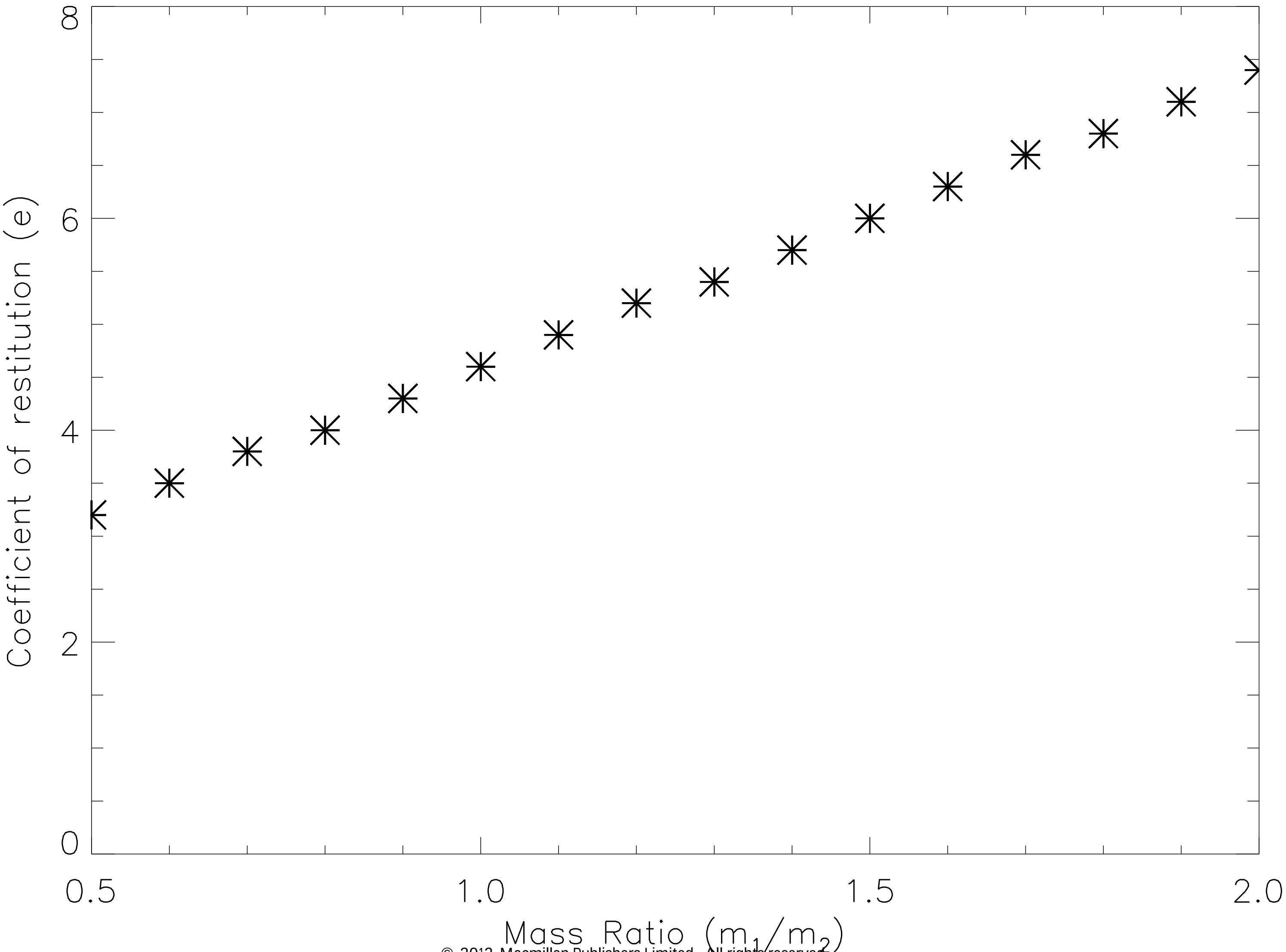
8
6
4
2
0
Coefficient of restitution (e)
0.5
1.0
1.5
2.0
Mass Ratio (m_1/m_2)

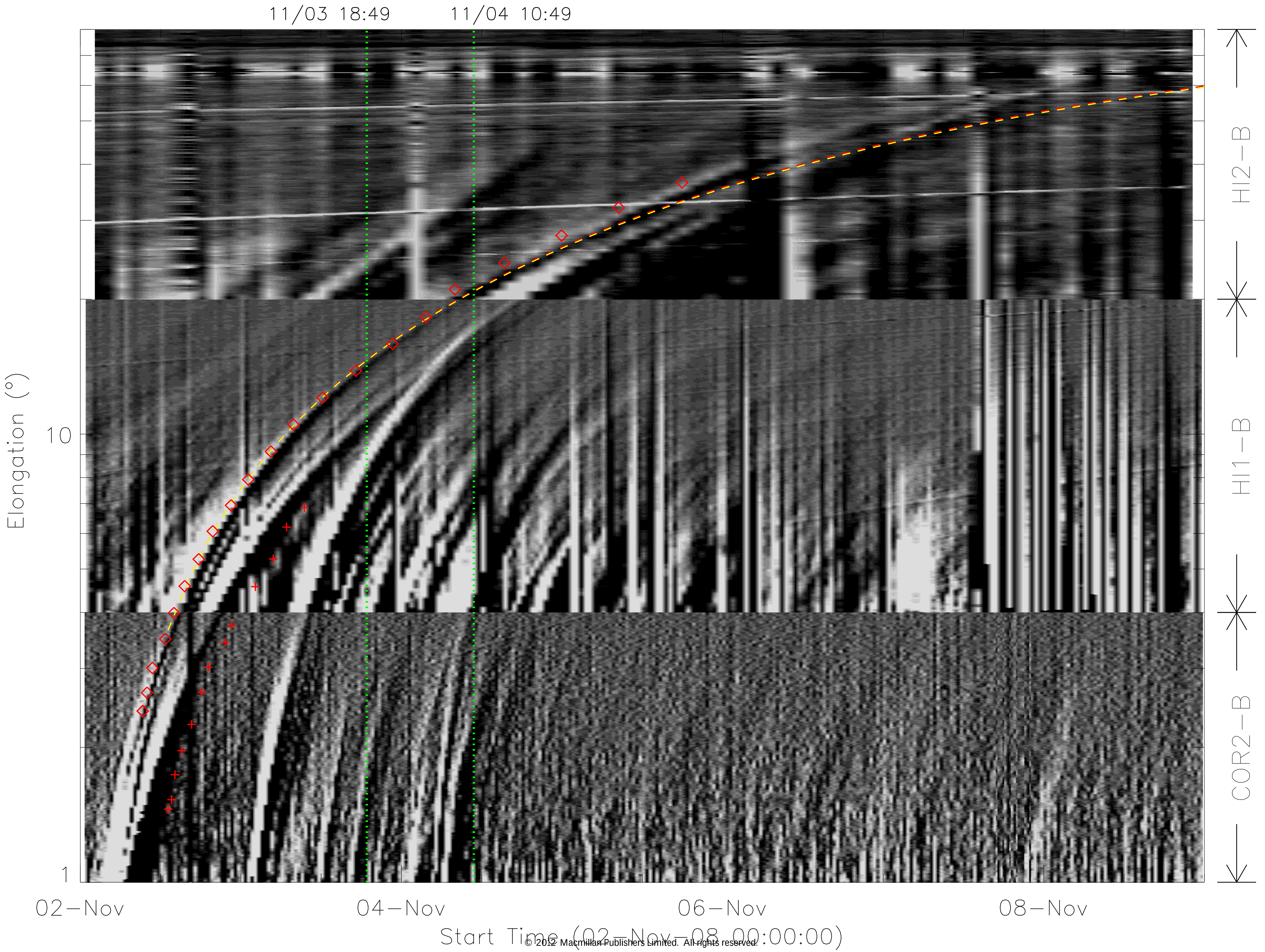

11/03 18:49
11/04 10:49
Elongation (°)
10
1
HI2−B
HI1−B
COR2−B
02−Nov
04−Nov
06−Nov
08−Nov
Start Time (02−Nov−08 00:00:00)

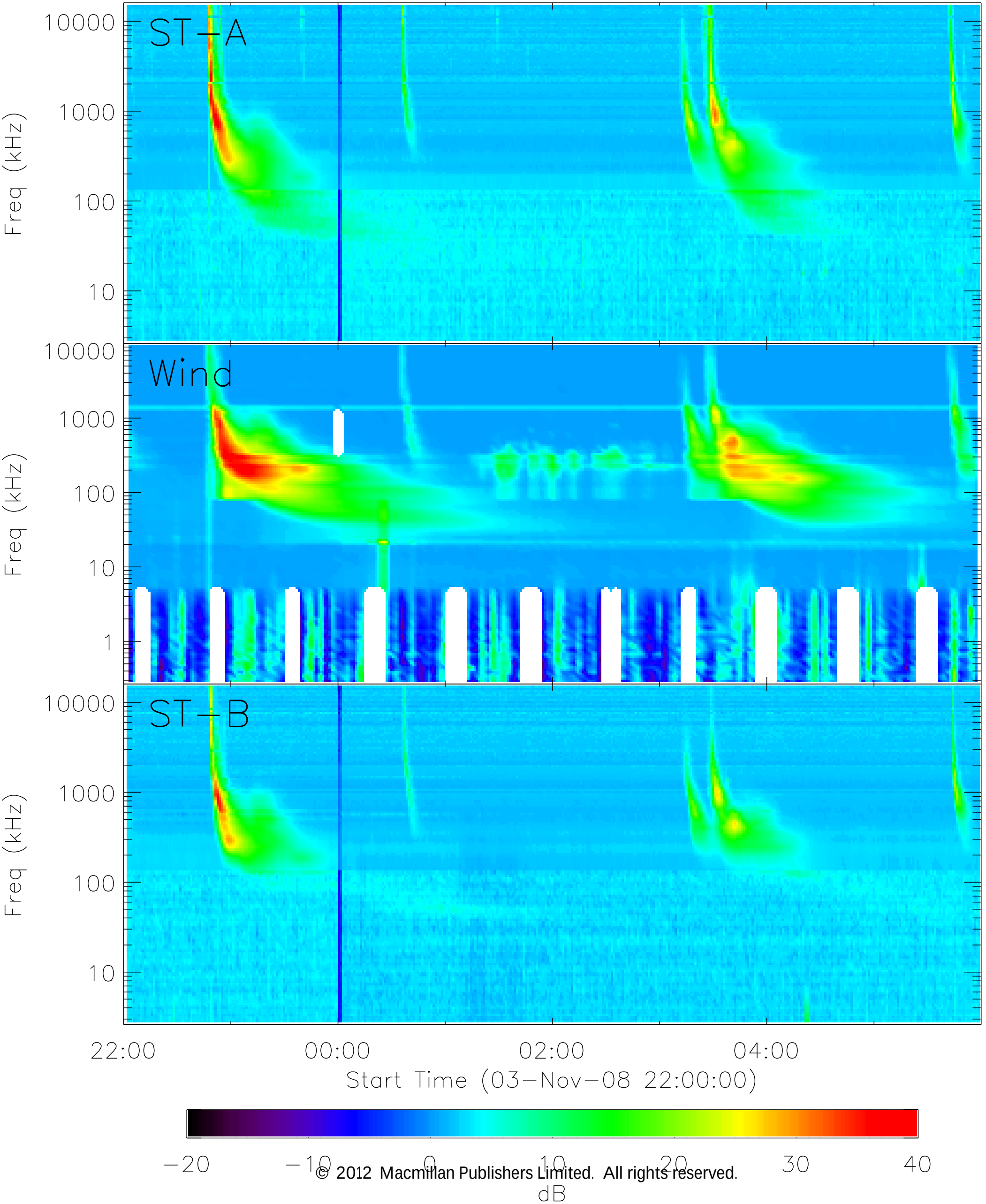
ST−A
Wind
ST−B
Freq (kHz)
10000
1000
100
10
1
22:00
00:00
02:00
04:00
Start Time (03−Nov−08 22:00:00)
−20
−10
0
10
20
30
40
dB

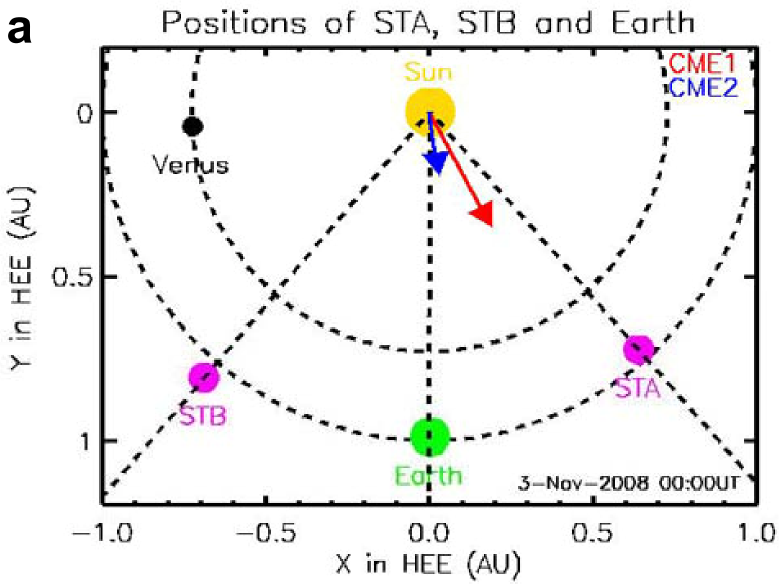
a
Positions of STA, STB and Earth
CME1
CME2
Sun
Venus
STB
STA
Earth
3-Nov-2008 00:00UT
Y in HEE (AU)
X in HEE (AU)
0
0.5
1
−1.0
−0.5
0.0
0.5
1.0

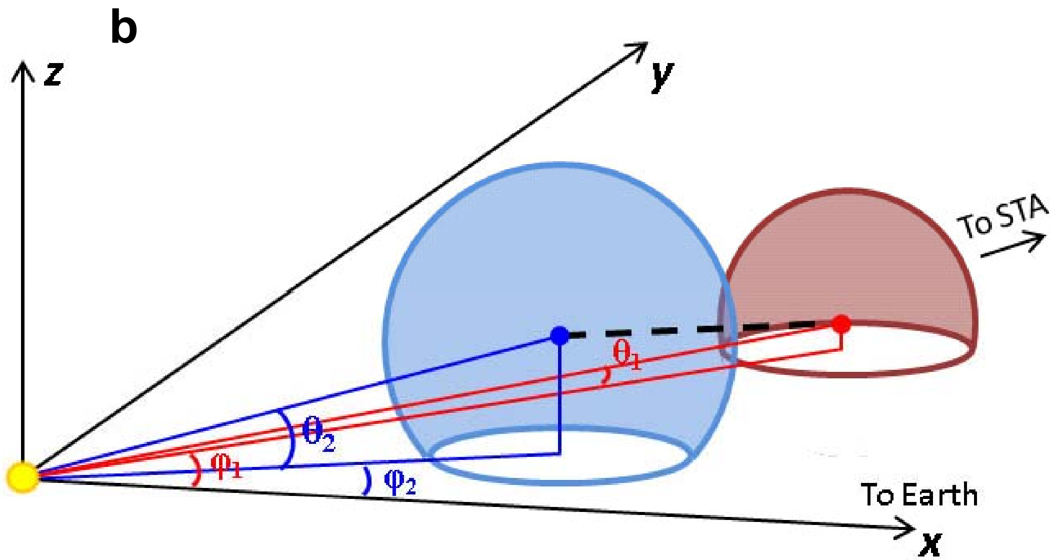
b
z
y
x
To STA
To Earth
θ1
θ2
φ1
φ2